

# Lawrence Berkeley National Laboratory

## LBL Publications

**Title**

GEOPHYSICAL TECHNIQUES FOR CO<sub>2</sub> PLUME MONITORING

**Permalink**

<https://escholarship.org/uc/item/4hz4t6gq>

**Authors**

Gasperikova, Erika  
Daley, Thomas  
Wang, Zan  
et al.

**Publication Date**

2017-10-31

Peer reviewed



# GEOPHYSICAL TECHNIQUES FOR CO<sub>2</sub> PLUME MONITORING

## TECHNICAL REPORT

Erika Gasperikova<sup>1</sup>, Thomas Daley<sup>1</sup>, Zan Wang<sup>2</sup>, Robert Dilmore<sup>2</sup>, William Harbert<sup>2</sup>, Lianjie Huang<sup>3</sup>, Kai Gao<sup>3</sup>, Ting Chen<sup>3</sup>, Miao Zhang<sup>3</sup>, Delphine Appriou<sup>4</sup>, Xianjin Yang<sup>5</sup>, Thomas Buscheck<sup>5</sup>, Kayyum Mansoor<sup>5</sup>, Susan Carroll<sup>5</sup>, Catherine Yonkofski<sup>4</sup>, Timothy Johnson<sup>4</sup>, Jeffrey Burghardt<sup>4</sup>, Christopher Strickland<sup>4</sup>, Christopher Brown<sup>4</sup>

[egasperikova@lbl.gov](mailto:egasperikova@lbl.gov), 510-486-4930

<sup>1</sup> Lawrence Berkeley National Laboratory

<sup>2</sup> National Energy Technology Laboratory

<sup>3</sup> Los Alamos National Laboratory

<sup>4</sup> Pacific Northwest National Laboratory

<sup>5</sup> Lawrence Livermore National Laboratory



October 2017

## **Disclaimer**

This document was prepared as an account of work sponsored by the United States Government. While this document is believed to contain correct information, neither the United States Government nor any agency thereof, nor The Regents of the University of California, nor any of their employees, makes any warranty, express or implied, or assumes any legal responsibility for the accuracy, completeness, or usefulness of any information, apparatus, product, or process disclosed, or represents that its use would not infringe privately owned rights. Reference herein to any specific commercial product, process, or service by its trade name, trademark, manufacturer, or otherwise, does not necessarily constitute or imply its endorsement, recommendation, or favoring by the United States Government or any agency thereof, or The Regents of the University of California. The views and opinions of authors expressed herein do not necessarily state or reflect those of the United States Government or any agency thereof or The Regents of the University of California.

Ernest Orlando Lawrence Berkeley National Laboratory is an equal opportunity employer.

## Table of Contents

INTRODUCTION.....	1
(1) Seismic monitoring .....	1
1.1 Introduction .....	1
1.2 3D/4D Surface Seismic.....	2
1.3 Data Acquisition and Processing.....	3
1.4 Parameters important to seismic monitoring.....	5
1.5 Workflow for Modeling of Seismic Monitoring .....	5
1.6 Rock physics modeling .....	6
1.7 Forward seismic modeling .....	10
1.8 2D seismic numerical modeling using acoustic-wave propagation in anisotropic media .....	12
1.9 Fast detection and location of induced microseismicity for CO <sub>2</sub> injection monitoring.....	15
1.10 References .....	17
(2) Gravity Modelling .....	20
2.1 Introduction .....	20
2.2 Gravity Forward Modeling .....	22
2.3 References .....	27
(3) Electrical and electromagnetic methods.....	28
3.1 Introduction .....	28
3.2 EM techniques for resistive targets .....	32
3.3 EM techniques for conductive targets .....	35
3.4 Electrical Resistance Tomography (ERT) .....	39
3.5 Surface ERT for conductive targets .....	39
3.6 Magnetotelluric method (MT) .....	43
3.7 AMT for conductive targets .....	45
3.8 References .....	47
(4) Methodology for Incorporating ERT Monitoring Data into DREAM.....	49
4.1 Overview .....	49

4.2 DREAM-E4D Workflow.....	51
4.3 References .....	54
SUMMARY.....	55
ACRONYMS .....	57
ACKNOWLEDGMENTS.....	58

## **INTRODUCTION**

This report considers the application of number of different indirect (remote sensing) geophysical techniques for monitoring geologic sequestration of CO<sub>2</sub> in brine-bearing formations. The time-lapse monitoring using seismic, gravity, electrical and electromagnetic techniques is described. Geophysical models used for numerical modeling are based on flow simulations of various CO<sub>2</sub> sequestration scenarios. Different monitoring approaches are suitable for a site characterization prior to CO<sub>2</sub> injection, for monitoring while injecting CO<sub>2</sub>, or for a post-injection stage. Basic principles of each technique are described. Workflows are described using various examples. Each of the techniques is sensitive to a different subsurface property. The seismic velocity depends on the bulk and shear modulus and density, the gravity response depends on density, and the electrical resistivity is sensitive to changes in formation properties such as porosity, pore fluid resistivity, and fluid saturation. For this reason these techniques are complementary to each other, and when used together they could provide improved characterization of the subsurface. In addition to individual techniques, incorporating an electrical resistance tomography (ERT) into DREAM (Designs for Risk Evaluation and Management) tool is also described.

## **(1) SEISMIC MONITORING**

### **1.1 Introduction**

Seismic monitoring utilizes seismic wave propagation in the earth (elastic waves) to determine changes in subsurface physical properties, and is typically the key monitoring tool for CO<sub>2</sub> storage projects. Seismic monitoring includes many types of data acquisition and analysis including passive monitoring of natural sources, i.e. microseismic events, and data acquisition with active (man-made) sources. Large-scale use of active-source seismic began in the early 1900's as a tool for resource exploration, and grew in both industrial application and academic research through the 20<sup>th</sup> century. Seismic monitoring is most often done from the surface generating either 2D 'lines' or 3D 'volumes' of data. This data is typically processed to generate images of reflecting interfaces or 'horizons', and then analyzed for the properties of those horizons that can be related to rock properties through rock physics models. A subset of seismic monitoring includes data recorded in boreholes, e.g., vertical seismic profiles (VSP). 3D surface seismic is probably the most advanced (and most expensive) method. When 3D seismic is used for repeated monitoring of the same site, it is termed '4D' seismic (with repeats over calendar time being the fourth dimension).

## 1.2 3D/4D Surface Seismic

3D seismic is acquired by recording data from sources and sensors covering a 2D area (in a grid or other pattern) and recording for a time period which allows the waves to reflect from the deepest horizons of interest – typically ~10 seconds of seismic travel time. The initial 3D images typically have time as the third dimension (along with x and y in meters or latitude and longitude on the surface). These ‘time sections’ are then converted to ‘depth sections’ using the inferred velocity of the subsurface materials. The depth section provides a true 3D image of reflecting horizons in the subsurface. Figure 1.1 shows an example 3D seismic data cube from a marine seismic survey.

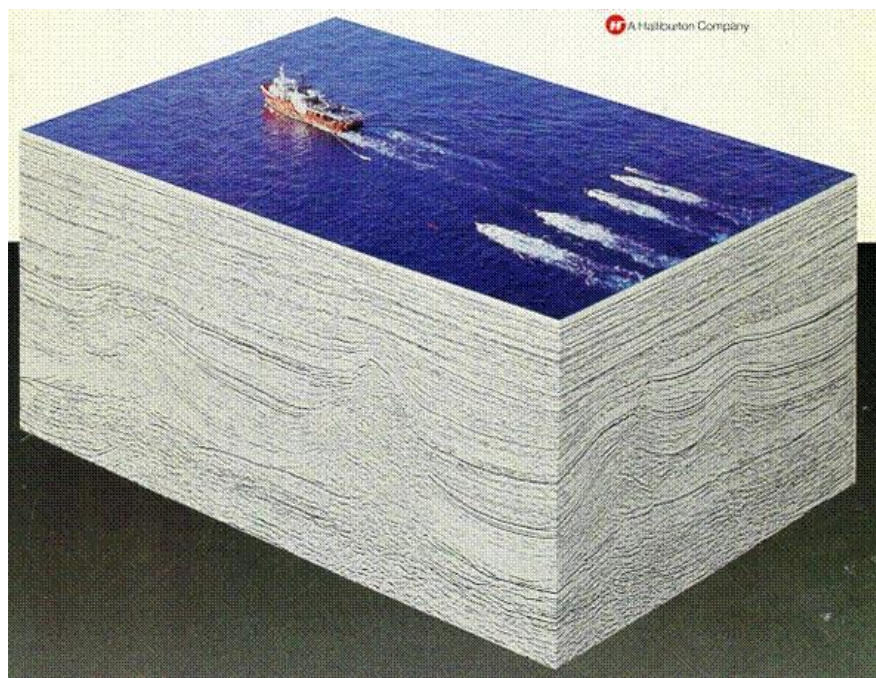


**Figure 1.1.** An example 3D seismic data volume with a photo of marine seismic data acquisition on the surface. Many coherent seismic reflections can be seen on the two sides of the data cube. From SEP, 2017.

The use 4D seismic to monitor injected CO<sub>2</sub> is best demonstrated by the Sleipner project which has been conducting 3D seismic surveys over an increasing volume of injected CO<sub>2</sub> since the mid 1990’s. An example of the Sleipner results is shown in Figure 1.2 which has 2D ‘slices’ of the 3D data for both vertical (right) and horizontal (map view) (lower left). The results shown in Figure 1.2 are for seven surveys over 14 years (through 2008) and monitoring at the site continues to the present (2017). Sleipner is an example of marine 3D seismic in which data is acquired by a ship (or multiple ships) deploying seismic sources and sensors in the ocean (Figure 1.1).

## Sleipner 4D Seismic

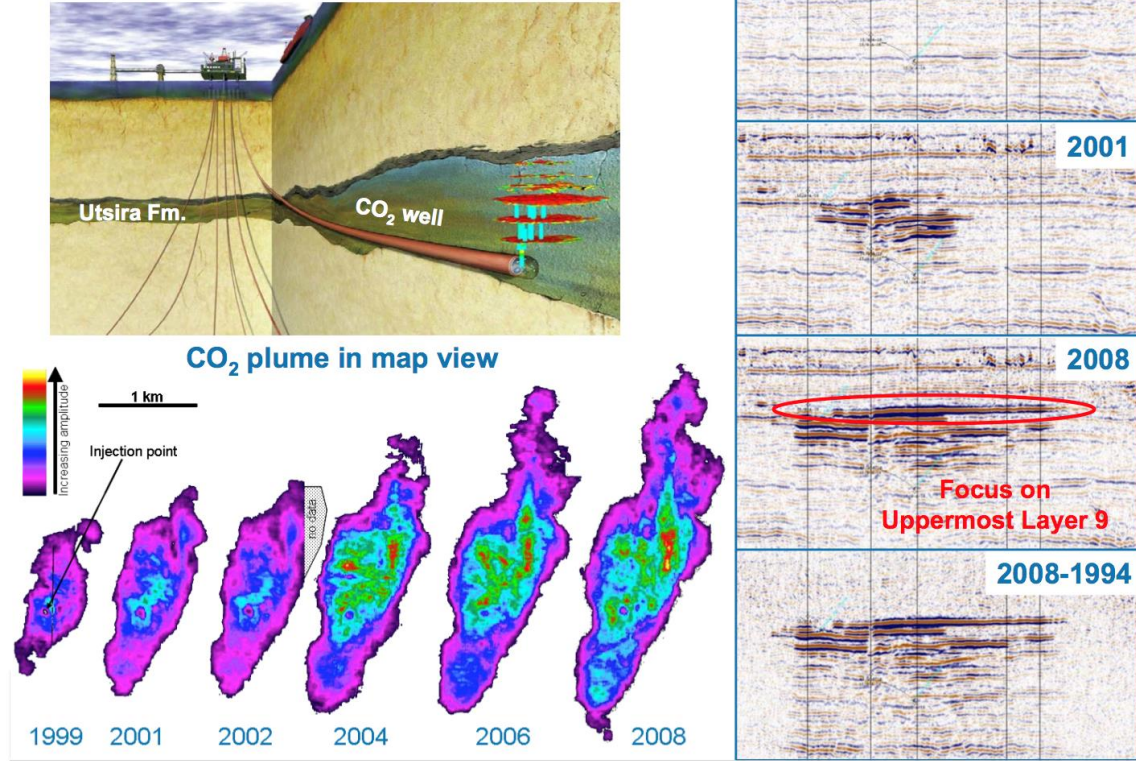


**Figure 1.2.** 4D seismic monitoring for the Sleipner storage project. Upper left shows a schematic of the injection into the Utsira formation with the rising buoyant CO<sub>2</sub> plume (blue and red). Right side figure shows a series of 2D vertical slices through the 3D data volume and through the injected CO<sub>2</sub> plume with the changing reflection amplitude clearly visible. The lower left is a series of horizon slices through the top layer containing CO<sub>2</sub> (layer 9 as indicated on the 2008 vertical slice) and plotted to show the interpreted extent of the amplitude change caused by CO<sub>2</sub> (purple, blue, green and red indicate different reflection amplitude changes). Figure courtesy P. Ringrose, see also Chadwick et al. (2010).

### 1.3 Data Acquisition and Processing

In general seismic monitoring data can be divided into marine and land surveys. Seismic data acquisition is a field rich in research with many books and journal articles published (see library.seg.org; e.g., Evans, 1997) and similarly the processing of seismic data has its own literature (e.g., Yilmaz, 2001). There are distinct differences in both data acquisition and processing between marine and land data. However, in the simplest conceptual model, both marine and land acquisition can be considered as a group of seismic sensors recording the waves generated by a single seismic source, as in Figure 1.3.

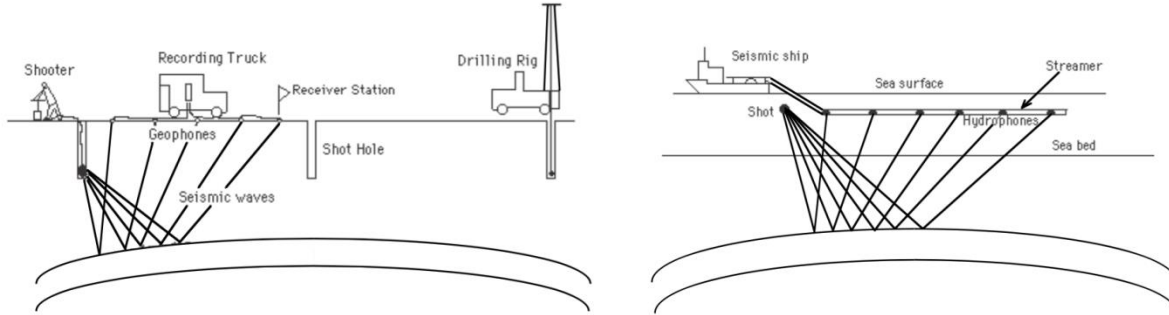


**Figure 1.3.** Schematic of surface seismic data acquisition for land (left) and marine (right) environments. The land acquisition shows the use of an explosive source deployed with a shot-hole drilling rig and surface geophone sensors connected to a recording truck. The marine acquisition shows a towed ‘array’ of hydrophone sensors and a shot source (typically compressed air ‘guns’) also towed from the seismic ship. Figures from Evans (1997).

The data shown in Figure 1.3 is acquired as shot ‘gathers’, with one source,  $S_1$ , and many receivers,  $R_1-R_N$ . A key step in imaging the reflecting interfaces is converting the shot gathers to common midpoint (CMP) gathers, as shown in Figure 1.4. For each CMP point on a reflecting horizon, many source-receiver pairs are ‘stacked’ together to create the CMP value. The number of traces stacked is called the ‘fold’ and is a measure of data quality (where larger fold is generally better quality data). Connecting the CMP points in depth for each reflecting layer leads to defining the location of a CMP ‘trace’ – the equivalent seismic recording – and this CMP trace is what is used to build a final image, such as in Figures 1.1 and 1.2.

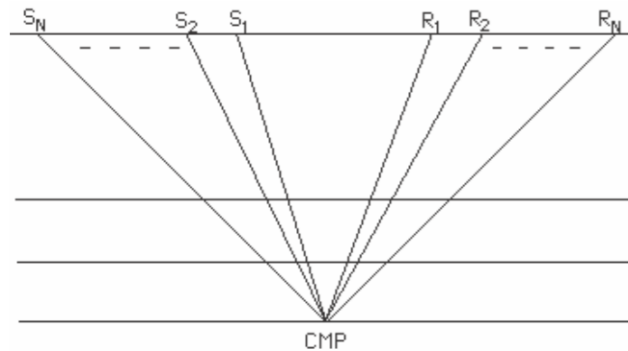


**Figure 1.4.** Schematic of surface seismic data from many sources ( $S_1$  to  $S_N$ ) and many receivers ( $R_1$  to  $R_N$ ) arranged so that they have a common midpoint (CMP) for horizontal reflecting interfaces. From Evans (1997).

## **1.4 Parameters important to seismic monitoring**

In practice, allowing for the variable geometry of acquisition (the true x, y, z location of both sources and sensors) is a key initial step in data processing. Another very important task in data processing is determining the seismic wave velocity of each layer. While conceptual models often assume constant layer velocity, in practice the velocity is a 3-dimensional (3D) variable as are the layer interface locations. Thus determining the velocity ‘model’ – a 3D description of velocity in the subsurface – is crucial to proper use of seismic data. Initially, seismic velocity is determined from the data itself, with other information (such as well measurements) added as available. The seismic velocity depends on the bulk and shear modulus and density (see rock physics section). These three parameters uniquely determine both P-wave and S-wave velocities for isotropic media. Inversely, obtaining P-wave and S-wave velocities from seismic monitoring data allows determination of elastic moduli (e.g., bulk and shear moduli) and density. Then, using rock physics relationships; reservoir parameters such as fluid saturation, porosity and pressure can be determined from the elastic moduli.

In practice, the use of seismic monitoring data to understand reservoir properties is usually a loop between modeling of the data and processing/analysis of the data. For example, the reflection amplitude change shown in Figure 1.2 can be, and has been, inverted for CO<sub>2</sub> saturation in work which includes forward modeling (e.g., flow modeling in Chadwick and Noy, 2011). Because of the large number of reservoir properties impacting the seismic response, as well as varying complexity in rock physics models, forward modeling is important to increase confidence in quantitative interpretations.

## **1.5 Workflow for Modeling of Seismic Monitoring**

Time-lapse seismic data analysis has been used at several CO<sub>2</sub> sequestration sites as an essential method for site characterization, imaging subsurface CO<sub>2</sub> plume migration and detecting potential CO<sub>2</sub> leakage. Monitoring in the aquifer above the primary seal is important for early detection of CO<sub>2</sub> leakage from the storage reservoir. Forward modeling of seismic data can be used to assess the ability of seismic methods for CO<sub>2</sub> leakage detection. We develop a workflow for forward modeling of seismic data, including constructing seismic velocity models using flow simulation results, modeling of synthetic seismic data followed by a basic processing sequence and analysis of stacked migrated synthetic seismic data. FutureGen 2.0 leakage simulations (Williams et al., 2014) are used to illustrate the process of forward modeling and analysis of synthetic seismic monitoring data (Figure 1.5).

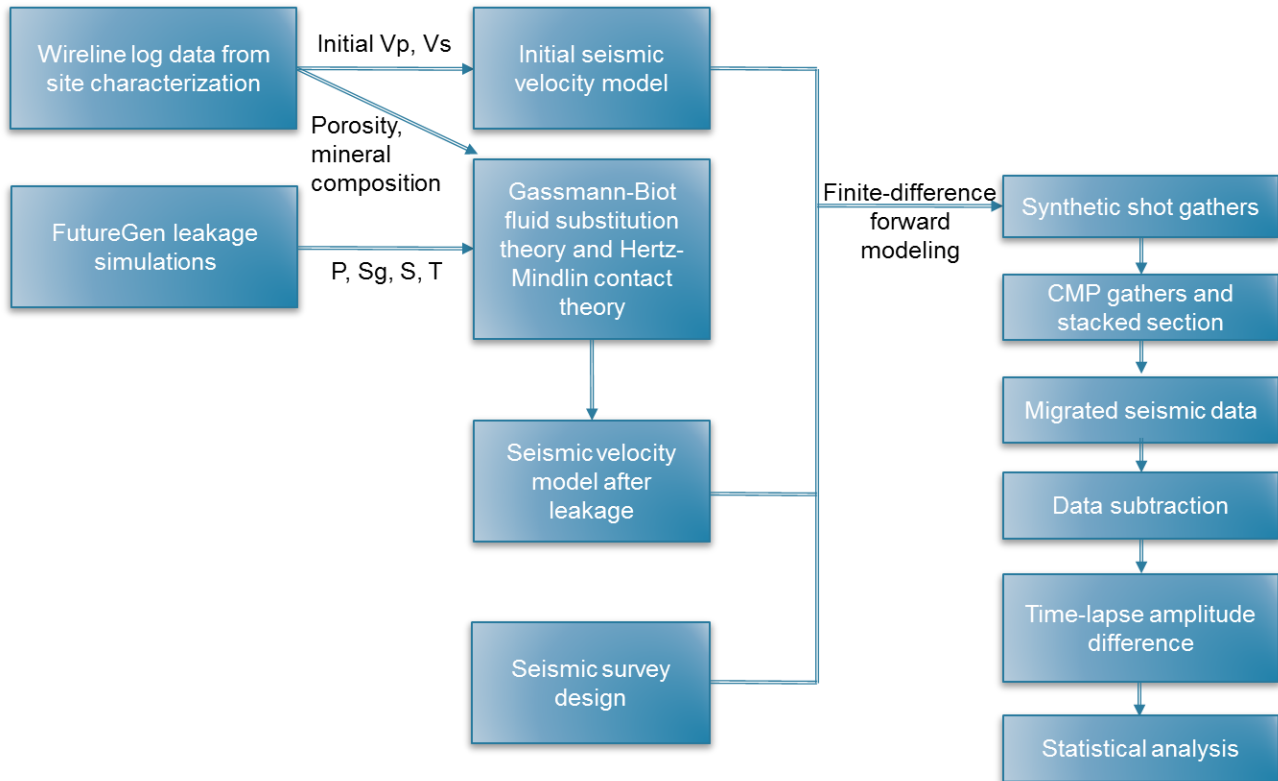


**Figure 1.5.** Schematic flow chart of forward modeling and analysis of synthetic seismic monitoring data

## 1.6 Rock physics modeling

To model the synthetic time-lapse seismograms, seismic velocity models need to be constructed at each time step. The initial seismic velocity model (i.e., before the CO<sub>2</sub> leakage) was constructed using the processed wireline log data (P- and S-wave slowness measurements) from the initial stratigraphic borehole (FutureGen Industrial Alliance, 2012). The slowness measurements are averaged over the interval of each stratigraphic unit. The seismic velocity for each stratigraphic unit is calculated as the reciprocal of the averaged slowness.

For the simulated CO<sub>2</sub> leakage scenarios at the FutureGen 2.0 site (Williams et al., 2014), changes in seismic velocity due to CO<sub>2</sub> leakage from the storage reservoir are calculated at each time step based on the Gassmann-Biot fluid substitution theory (Gassmann, 1951) and the Hertz-Mindlin contact theory (Mindlin, 1949). The instantaneous velocity field in the model domain is related to moduli and density of the rock by:

$$V_p = \sqrt{\frac{K_{sat} + 4\mu/3}{\rho_{sat}}}$$

$$V_s = \sqrt{\frac{\mu}{\rho_{sat}}}$$

Where  $V_p$  and  $V_s$  are the P-wave and S-wave velocities;  $K_{sat}$  is the bulk modulus of the rock after fluid substitution;  $\mu$  is the shear modulus of the rock, which is constant during the fluid substitution in the Gassmann-Biot theory.  $\rho_{sat}$ , the density of rock after fluid substitution is calculated as:

$$\rho_{sat} = \rho_{initial} + \varphi(\rho_{fluid}^{update} - \rho_{fluid}^{initial})$$

Where  $\rho_{initial}$  is the initial bulk density of the rock, which can be obtained from the density log in the site characterization;  $\rho_{fluid}^{initial}$  and  $\rho_{fluid}^{update}$  are the densities of the fluid phase before and after CO<sub>2</sub> invasion, respectively.

The bulk modulus of the rock after fluid substitution ( $K_{sat}$ ) at each node in the model domain is estimated using the low frequency Gassmann equation (Gassmann, 1951):

$$K_{sat} = K_{frame} + \frac{\left(1 - \frac{K_{frame}}{K_{mineral}}\right)^2}{\frac{\varphi}{K_{fl}} + \frac{1 - \varphi}{K_{mineral}} - \frac{K_{frame}}{K_{mineral}^2}}$$

where  $K_{frame}$ ,  $K_{mineral}$ , and  $K_{fl}$  are the bulk moduli of dry rock frame, mineral grains and effective pore fluid (mixed pore fluid phases), respectively;  $\varphi$  is the porosity of the rock as a volume fraction, which can be obtained either from the wireline log data or the input parameters of the flow simulations.

The bulk modulus and density of effective pore fluid ( $K_{fl}$  and  $\rho_{fl}$ ) can be estimated by inverse bulk modulus averaging and arithmetic averaging of densities of the separate fluid phases (brine phase and supercritical CO<sub>2</sub> phase), respectively (Kumar, 2006):

$$\frac{1}{K_{fl}} = \frac{S_w}{K_{brine}} + \frac{S_g}{K_{co2}} \quad \text{and} \quad \rho_{fl} = S_w \rho_{brine} + S_g \rho_{co2}$$

where  $S_g$  is the CO<sub>2</sub> saturation (as volume fraction) and  $S_w$  ( $= 1 - S_g$ ) is the brine saturation. The bulk moduli and densities of pure brine and supercritical CO<sub>2</sub> ( $K_{brine}$ ,  $K_{co2}$  and  $\rho_{brine}$ ,  $\rho_{co2}$ ) are calculated as a function of temperature, pore pressure and salinity using relationships developed by Batzle and Wang (1992). The input parameters (i.e., temperature, pore pressure, salinity and CO<sub>2</sub> saturation) at each node in the model domain at each time step are obtained from flow simulation outputs. Example outputs from the FutureGen 2.0 leakage simulations at t= 20 years in the 20-year leakage scenario are shown in Figure 1.6.

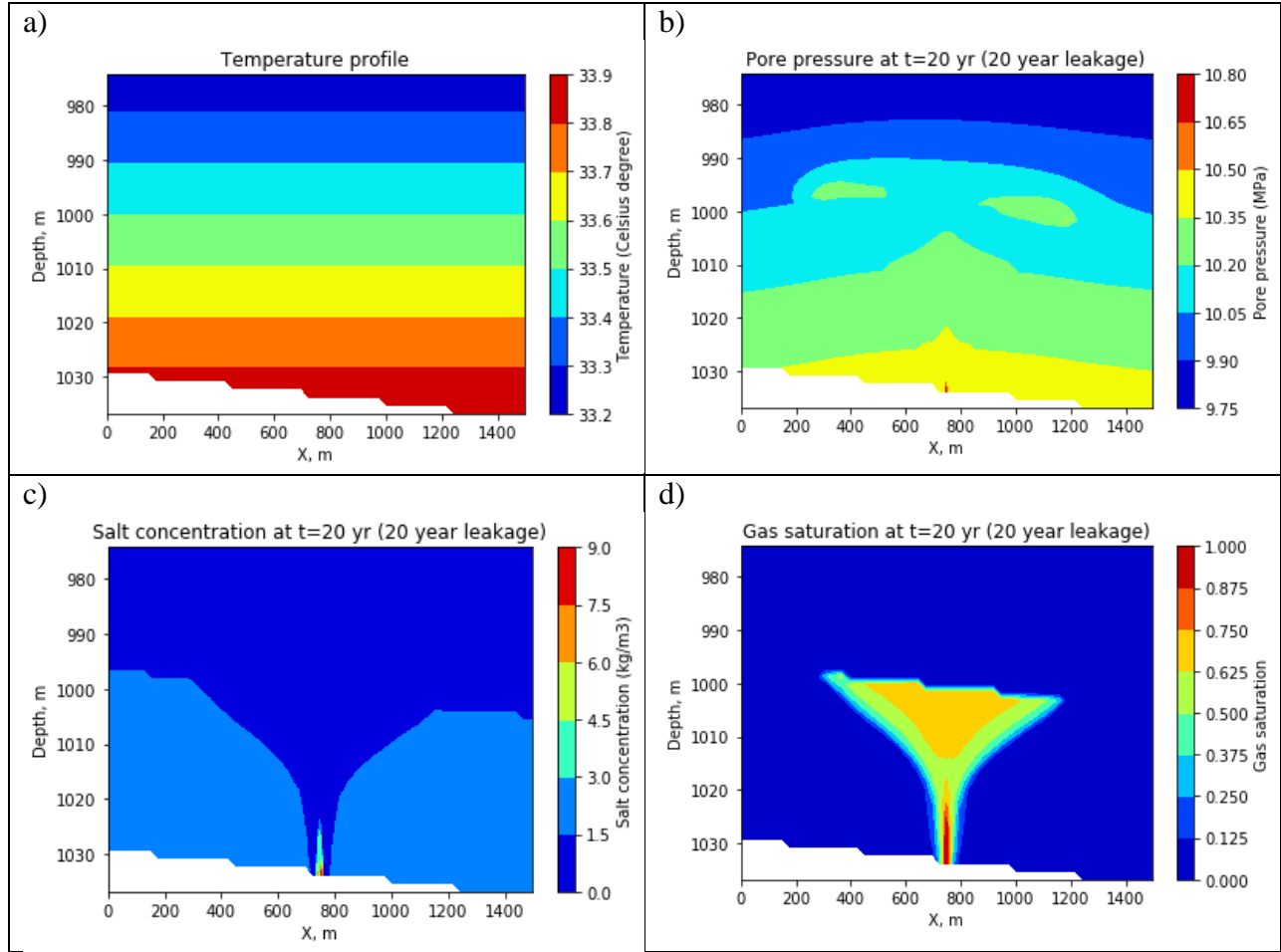


**Figure 1.6.** Example outputs from FutureGen 2.0 leakage simulations: a) temperature; b) pore pressure; c) salt concentration; d) CO<sub>2</sub> saturation profiles for a x-z cross section at y=0 location in the leakage zone (Ironton Sandstone) and the unit directly above the leakage zone (Davis Dolomite) at t =20 years in the 20-year leakage scenario.

The bulk and shear moduli of mineral grains ( $K_{mineral}$  and  $\mu_{mineral}$ ) are estimated by taking Voigt-Reuss-Hill averaging (Hill, 1952) of the mineral constituents. The mineral composition of each stratigraphic unit (volume fraction), is obtained from the processed wireline log data in the site characterization. Computed elemental analysis lithology from the wireline log data indicates that the mineral constituents at the FutureGen 2.0 site are quartz, dolomite, calcite, K-feldspar, kaolinite, illite and pyrite. The moduli of the mineral constituents can be obtained from papers and textbooks (e.g., Mavko et al., 2009; Mondol et al., 2008; Roach et al., 2015).  $K_{mineral}$  remains constant during the Gassmann fluid substitution.

$$k_{voigt} = \sum_{i=1}^n v_i * k_i; \quad k_{reuss} = \frac{1}{\sum_{i=1}^n v_i / k_i}; \quad K_{mineral} (\text{or } \mu_{mineral}) = 0.5 * (k_{voigt} + k_{reuss})$$

where  $v_i$  is the volume fraction and  $k_i$  is the bulk/shear modulus of mineral constituent i; n is the number of mineral constituents, which is 7 for the FutureGen 2.0 site.

The initial bulk modulus of the dry rock frame ( $K_{frame}^{initial}$ ) can be derived from the wireline log data by rewriting the Gassmann equation for  $K_{frame}$  (Zhu and McMechan, 1990) as

$$K_{frame}^{initial} = \frac{K_{sat}^{initial} \left( \frac{\varphi K_{mineral}}{K_{fluid}^{initial}} + 1 - \varphi \right) - K_{mineral}}{\frac{\varphi K_{mineral}}{K_{fluid}^{initial}} + \frac{K_{sat}^{initial}}{K_{mineral}} - 1 - \varphi}$$

where  $K_{sat}^{initial}$  is the initial bulk modulus of the wet rock, which can be derived from the wireline log data as  $K_{sat}^{initial} = \rho_{initial} [(V_p^{initial})^2 - \frac{4}{3} * (V_s^{initial})^2]$ . The other parameters are defined in the previous equations.

The effects of pore pressure changes on bulk modulus of dry rock frame are modeled based on the Hertz-Mindlin contact theory (Mindlin, 1949). The effective elastic properties of rock at critical porosity  $\varphi_c$  are given by:

$$K_{mc} = \left( \frac{C^2 (1 - \varphi_c)^2 \mu_{mineral}^2 p_d}{18\pi^2 (1 - v_s)^2} \right)^{1/3}$$

$$\mu_{mc} = \frac{5 - 4v_s}{5(2 - v_s)} \left( \frac{3C^2 (1 - \varphi_c)^2 \mu_{mineral}^2 p_d}{2\pi^2 (1 - v_s)^2} \right)^{1/3}$$

where  $p_d = p_c - p$  is the differential pressure calculated by subtracting the pore pressure ( $p$ ) from the confining pressure ( $p_c$ ). The pore pressure and the confining pressure are obtained from the flow simulation outputs and the wireline log data used in site characterization.  $v_s$  is the Poisson's ratio of the minerals;  $\varphi_c$  is the critical porosity and  $C$  is the average number of contacts per spherical mineral grain. Based on data by Murphy (Carcione et al., 2006; Murphy, 1982),  $C = 2.8/\varphi_c$ .

The effective bulk and shear moduli of dry rock frame at a different porosity  $\varphi$  can be estimated using the modified Hashin-Strikman lower bound (Dvorkin and Nur, 1996) based on the original Hashin-Strikman lower bound (Hashin and Shtrikman, 1963).

$$K_{frame} = \left[ \frac{\frac{\varphi}{\varphi_c}}{K_{mc} + \frac{4}{3}\mu_{mc}} + \frac{1 - \frac{\varphi}{\varphi_c}}{K_{mineral} + \frac{4}{3}\mu_{mc}} \right]^{-1} - \frac{4}{3}\mu_{mc}$$

$$\mu = \left[ \frac{\frac{\varphi}{\varphi_c}}{\mu_{mc} + \frac{\mu_{mc}}{6}(\frac{9K_{mc} + 8\mu_{mc}}{K_{mc} + 2\mu_{mc}})} + \frac{1 - \frac{\varphi}{\varphi_c}}{\mu_{mineral} + \frac{\mu_{mc}}{6}(\frac{9K_{mc} + 8\mu_{mc}}{K_{mc} + 2\mu_{mc}})} \right]^{-1} - \frac{\mu_{mc}}{6}(\frac{9K_{mc} + 8\mu_{mc}}{K_{mc} + 2\mu_{mc}})$$

where  $K_{\text{mineral}}$  and  $\mu_{\text{mineral}}$  are the bulk and shear moduli of mineral grains, respectively.

Figure 1.7 shows the predicted changes in seismic velocity from the rock physics modeling at  $t = 20$  years in the 20-year leakage scenario.

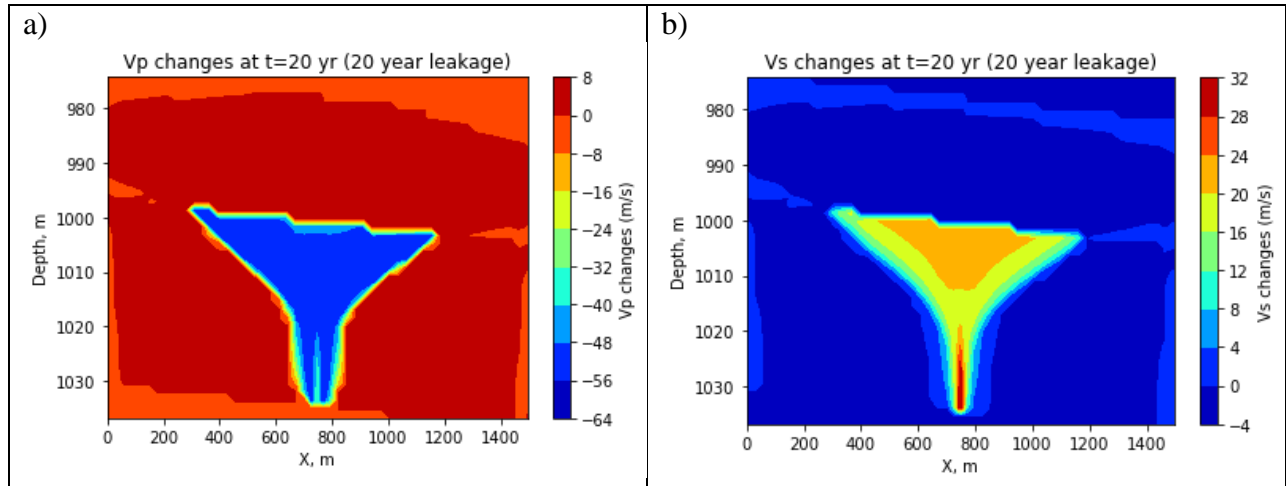


**Figure 1.7.** Predicted changes in seismic velocity: a) P-wave velocity changes; b) S-wave velocity changes at  $t = 20$  years in the 20-year leakage scenario.

### 1.7 Forward seismic modeling

Two-dimensional (2D) acoustic seismic modeling was performed to infer the CO<sub>2</sub> leakage. A 2D seismic line was shot through the constructed seismic velocity model at each time step. The 2D line is parallel to the x axis, at  $y=0$  location so that the imaged x-z cross section intersects the leakage point. The extent of the seismic velocity model in x and z directions are 1,490 m and 1,190 m, respectively. Along the 2D surface seismic line, there are 135 shots covering the x range of 80 m to 1,420 m and 299 receivers covering the x range of 0 m to 1,490 m. The shot point spacing is 10 m. The receiver station spacing is 5 m. The dominant frequency of the source wavelet, which is modeled as a Ricker wavelet, is 30 Hz. The sampling rate is 1 ms and the record length is 3 s. Synthetic shot gathers were generated using the 2D acoustic finite-difference modeling facility in the CREWES MATLAB Toolbox (Margrave, 2000). The computation time step in the finite-difference modeling is 0.2 ms and the computation grid is 5m×5m. The generated common shot gathers were converted to the common mid-point (CMP) gathers and the CMP stack was created. Then 2D depth migration was performed on the stacked section using the phase shift plus interpolation method implemented in the CREWES MATLAB Toolbox (Ferguson and Margrave, 2005). The post stack migrated seismic data at each time step are subtracted from the migrated synthetic data at the initial time step ( $t=0$ ), to get the time-lapse amplitude difference datasets. The outcomes of the forward seismic modeling (i.e., amplitude changes in the migrated synthetic seismic data) are used to infer the CO<sub>2</sub> leakage, which is a

combined effect of variations in geophysical parameters, including pore fluid type, pore fluid saturation and effective pressure. Figure 1.8 shows example outputs from the forward seismic modeling. Data in Figure 1.8a and Figure 1.8c are the post-stack, post-migration seismic data (amplitudes as a function of  $x$  and  $z$ ) within the depth window of the leakage zone (Ironton Sandstone) and the unit directly above the leakage zone (Davis Dolomite) ( $z=975\text{-}1035$  m) at  $t = 0$  (before the start of leakage) and  $t = 20$  years (since the leakage starts), respectively. The amplitude difference data at  $t = 20$  years are shown in Figure 1.8b. Figure 1.8d shows the percent amplitude changes at  $t = 20$  years in the whole model domain ( $z=0\text{-}1035$  m).

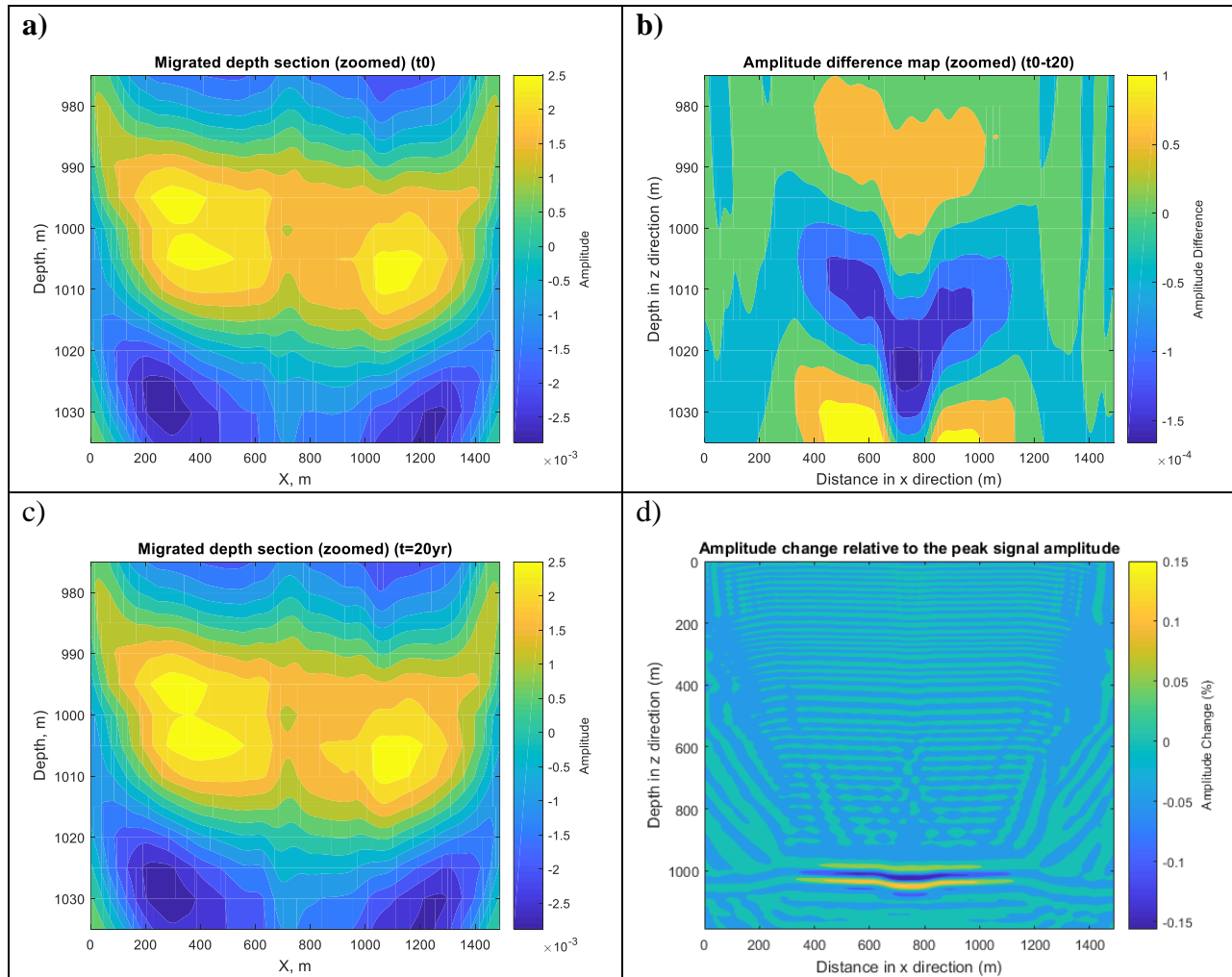


**Figure 1.8.** Example outputs from the forward seismic modeling. (a) Migrated depth section at  $t = 0$ , (c) migrated depth section at  $t = 20$  years, (b) amplitude difference map at  $t = 20$  years, and (d) percent amplitude changes at  $t = 20$  years in the whole model domain.

## 1.8 2D seismic numerical modeling using acoustic-wave propagation in anisotropic media

Acoustic-wave propagation in anisotropic media is considered as an approximation of elastic-wave propagation in anisotropic media when considering only compressional waves. Numerical modeling of acoustic-wave propagation in anisotropic media is a useful tool for studying seismic monitoring modeling of ROM models. When inhomogeneity, e.g., fault might play a significant role in a storage reservoir behavior it is necessary to image the subsurface with a higher accuracy. A pseudo-spectral method for 2D numerical modeling of acoustic-wave propagation in anisotropic media is used to study acoustic-wave propagation and scattering from a fault (Figure 1.9). The fault is considered as anisotropic medium - Tilted Transverse Isotropic (TTI) medium, with the Thomsen parameters within the fault  $\epsilon = 0.2$ ,  $\delta = 0.1$ , and TTI tilted angle  $\theta = 80.0^\circ$ .

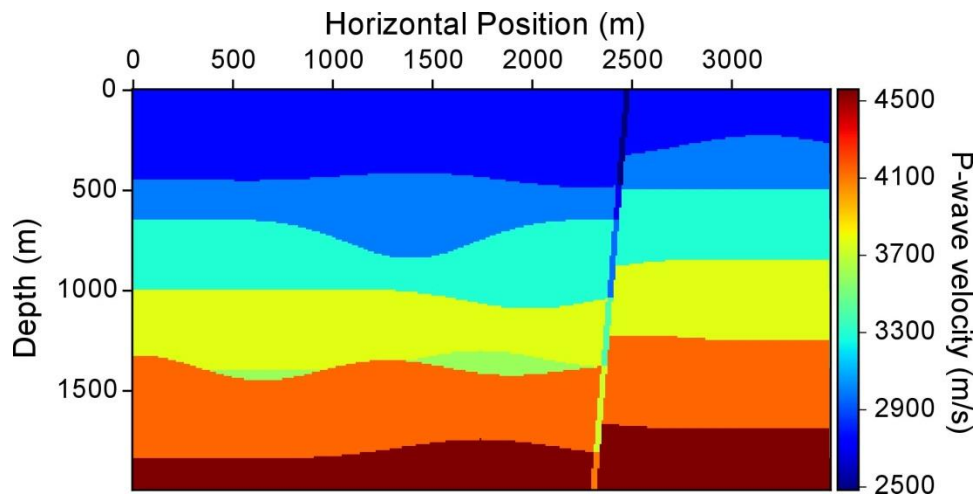


**Figure 1.9:** A 2D medium with a normal fault for numerical modeling of acoustic-wave propagation and scattering from the fault.

Figure shows a comparison of numerical modeling results of wavefield snapshots for acoustic-wave propagation in the model in Figure 1.9 when considering the fault as an isotropic and anisotropic medium, and their wavefield snapshot difference. The source wavelet is a Ricker source function with a center frequency of 30 Hz. The source is located at the horizontal position of 1,050 m at the top surface of the model. The numerical modeling results shown in Figure 1.10 demonstrate that the anisotropic properties in the fault can cause significant difference in wavefield snapshots and therefore, it is essential to properly account for anisotropic properties within the fault during seismic monitoring of possible CO<sub>2</sub> leakage through the fault zone.

Seismic reflection data are often used for seismic monitoring of possible CO<sub>2</sub> leakage through fault zones. Figure 1.11 displays seismic reflection data recorded at receivers located at the top surface of the model in **Figure 1.9** during numerical modeling of acoustic-wave propagation in the model in **Figure 1.9** when considering the fault is an isotropic medium (a) and an anisotropic

media (b), together with the seismogram difference in (c). **Figure 1.(c)** shows again that the difference between acoustic-wave scattering from the TTI fault and that from the isotropic fault is significant. This difference could be larger than that caused of CO<sub>2</sub> leakage.

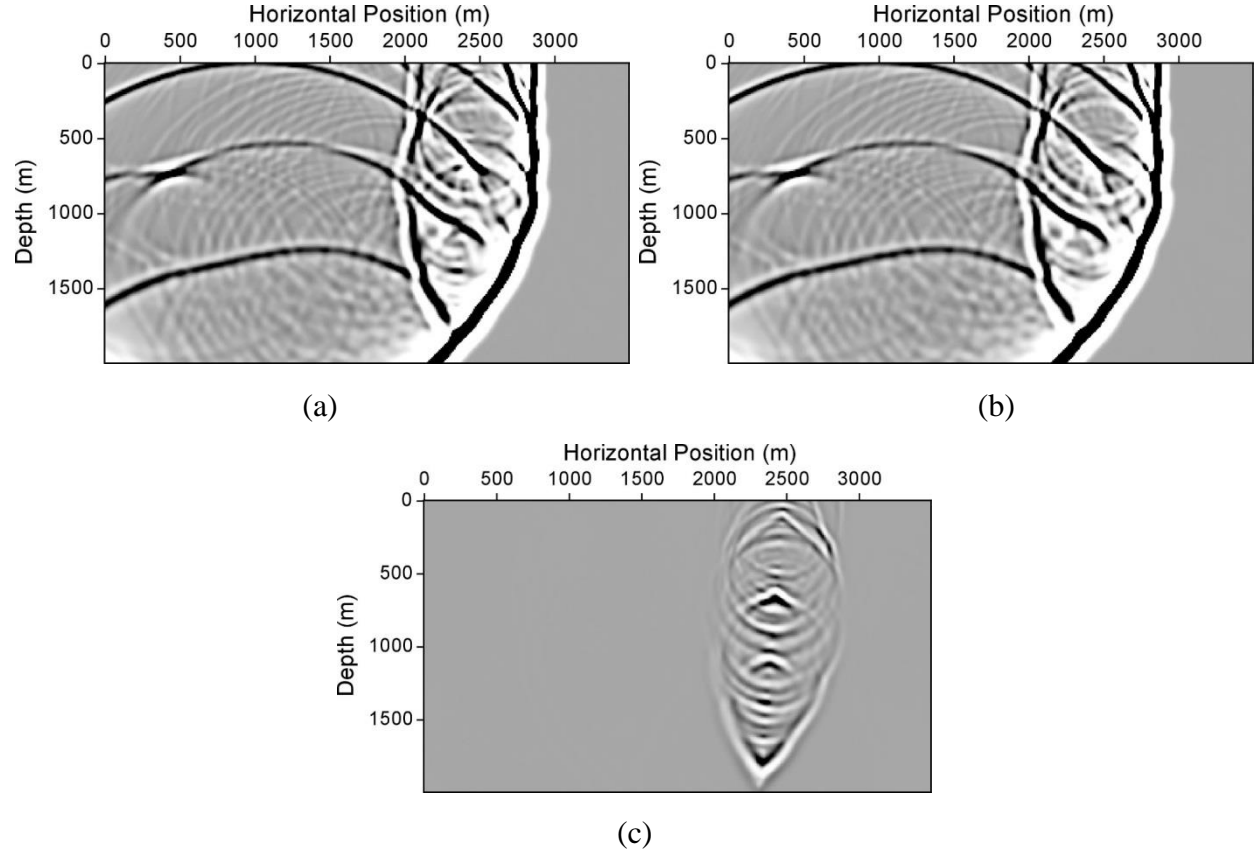


**Figure 1.10:** Snapshots of numerical modeling of acoustic-wave propagation in the model in **Figure 1.9** when considering the fault is an isotropic medium (a) and an anisotropic media (b), together with the snapshot difference in (c), for a source located at top surface of the model with the horizontal position of 1,050 m. Panels in (a)-(c) are plotted on the same scale.

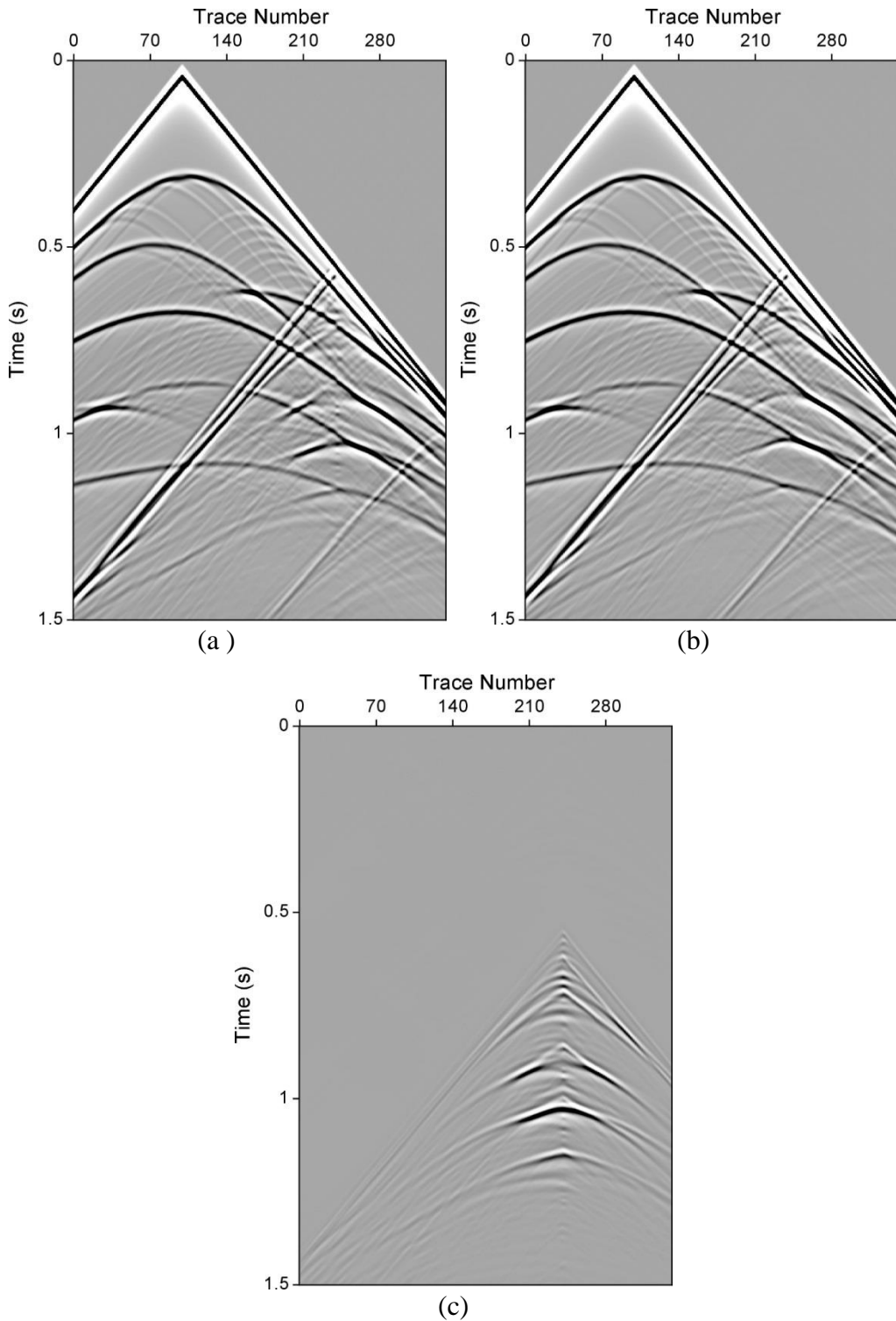


**Figure 1.11:** Seismograms at receivers located at the top surface of the model in Figure 1.9 obtained using numerical modeling of acoustic-wave propagation in the model in Figure 1.9 when considering the fault is an isotropic medium (a) and an anisotropic media (b), together with the seismogram difference in (c), for a source located at top surface of the model with the horizontal position of 1050 m. Panels in (a)-(c) are plotted on the same scale.

### 1.9 Fast detection and location of induced microseismicity for CO<sub>2</sub> injection monitoring

The injection of CO<sub>2</sub> into the underground during geological carbon storage may induce microseismic events as a result of stress and/or pore-pressure change. The induced microseismicity helps monitor CO<sub>2</sub> migration, and detect fault and cap rock leakage. Fast and accurate detection and location of induced microseismic events is crucial for the risk assessment and management for geological carbon storage. Below is a new tool for fast detection of CO<sub>2</sub>-injection-induced microseismic events. This tool is based on pre-calculated waveforms of a number of microseismic events and comparison of seismic waveforms of nearby microseismic events. A machine learning algorithm is employed to quickly detect and locate microseismic events from continuously recorded data.

In this tool, the first step is to pre-calculate waveforms for a group of microseismic events on a number of geophones (Figure a). Then, these waveforms are transformed into their envelopes (Figure b). By choosing a threshold and setting the value above the threshold to be 1 and the value below the threshold to be 0, these envelopes are further converted to images (Figure c). These steps simplify the data, and reduce the impact of noise. These pre-calculated images are then used to create a training dataset. By comparing the test data against the group of training dataset, using a machine learning algorithm (k-nearest neighbors algorithm) the detection test and the event location prediction is done for each seismic record. This algorithm measures the distance between test data and each of training data, and predicts the value for the test data based on the values of a few closest neighbors that have shortest distance.

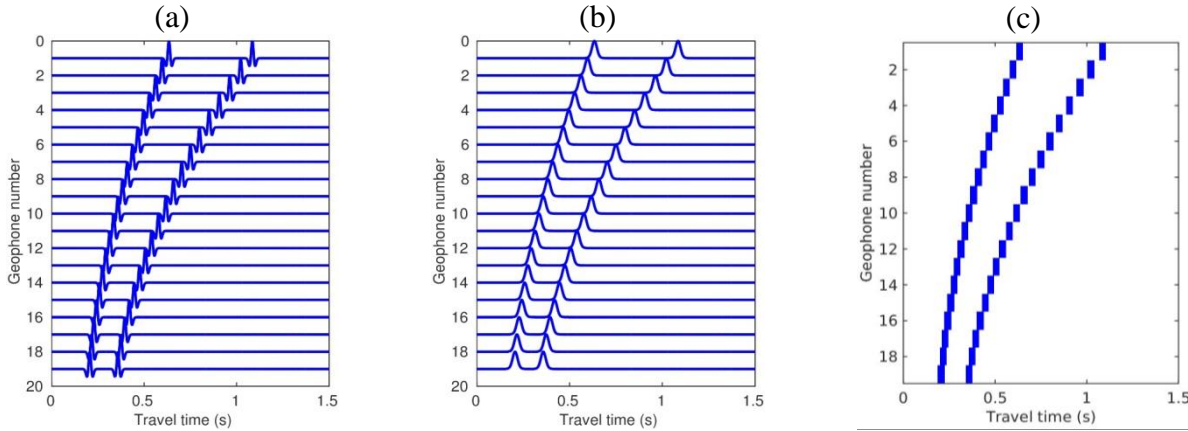


**Figure 1.12:** Illustration of seismic data processing steps: (a) waveform, (b) envelope, (c) image.

A synthetic example that uses a model for the Kimberlina site located in southern San Joaquin Valley, California is used to demonstrate the capability of this new tool. The model and a distribution of synthetic seismic events and geophones is shown in Figure a. There are 19

geophones from the depth of 0.2 to 2.0 km with a spacing of 100 m. A total of 369 synthetic microseismic events are distributed in the reservoir (depth 2.1 – 2.5 km) with a regular spacing interval of 50 m in both horizontal and vertical directions. Synthetic data images for seismic events at different locations show different patterns (Figure b-1.13c). For each synthetic event, three data images and three labels are put into training dataset. The data images include the cases for P plus S phases, only P phase, and only S phase. The labels include spatial location  $x$ ,  $z$ , and ‘Yes’ to classify that it is a seismic event. Besides synthetic events, the training dataset contains also non-event samples, which include a white image and some random noise images with labels of ‘No’ to indicate that they are not seismic events.

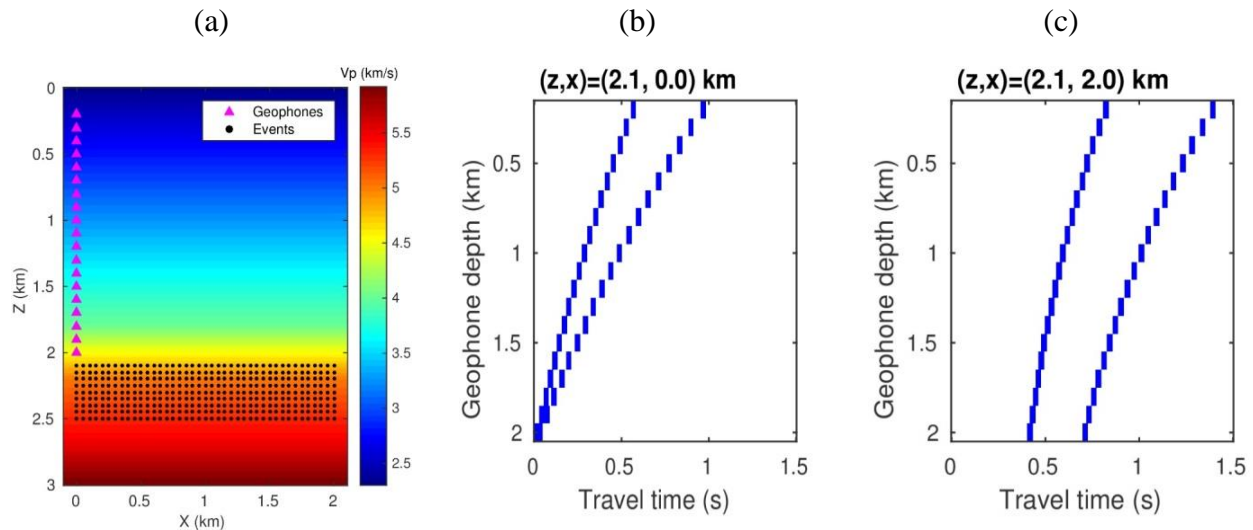


**Figure 1.13:** Synthetic example for training dataset. (a) Velocity model and distribution of microseismic events (black dots) and geophones (magenta triangles) for the Kimberlina site. (b-c) Two examples of training data for microseismic events at two different locations.

Examples in Figure 1.14 are some of this tool outputs. For a great range of seismic record, including imperfect data such as partial (Figure a) and noisy data (Figure b-1.14c), the tool performs well by predicting the locations of event close to their true locations. The standard deviation of spatial error is smaller than 50 m (Figure ).

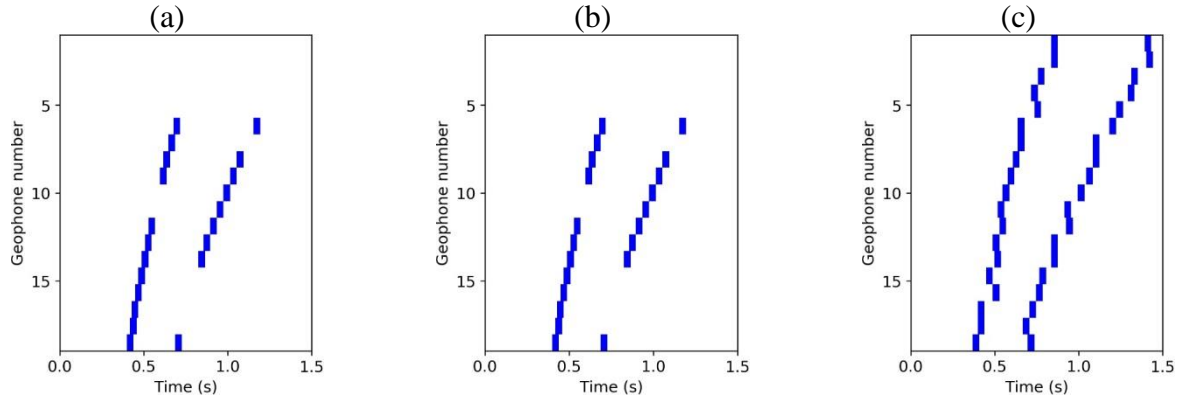


**Figure 1.14:** Synthetic test examples. (a) True location  $(x, z) = (1.98, 2.48)$  km, predicted location  $(x, z) = (2.00, 2.45)$  km. (b) True location  $(x, z) = (1.98, 2.48)$  km, predicted location  $(x, z) = (2.00, 2.45)$  km. (c) True location  $(x, z) = (1.98, 2.48)$  km, predicted location  $(x, z) = (1.90, 2.43)$  km.

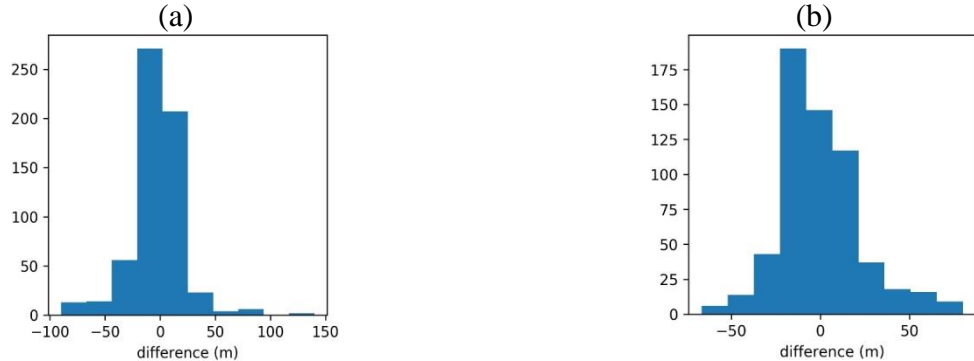


**Figure 1.15:** Difference between predicted and true locations for (a) x direction and (b) z direction.

## 1.10 References

- Alliance (FutureGen Industrial Alliance, Inc.) (2012). Borehole Completion and Characterization Summary Report for the Stratigraphic Well , Morgan County , Illinois. September 2012. Washington, D.C.
- Batzle, M., and Wang, Z. (1992). Seismic properties of pore fluids. *Geophysics* 57, 1396–1408. doi:10.1190/1.1443207
- Carcione, J.M., Picotti, S., Gei, D., and Rossi, G. (2006). Physics and seismic modeling for monitoring CO<sub>2</sub> storage. *Pure Appl. Geophys.* 163, 175–207.
- Chadwick, R.A., G. Williams, N., D.V. Clochard, K. Labat, S. Sturton, M-L. Buddensiek, M. Dillen, M. Nickel, A.L. Lima, R. Arts, F. Neele, and G. Rossi (2010). Quantitative analysis of time-lapse seismic monitoring data at the Sleipner CO<sub>2</sub> storage operation. *The Leading Edge*, 29, 170-177.

- Chadwick, R.A., and D.J. Noy (2011). History-matching flow simulations and time-lapse seismic data from the Sleipner CO<sub>2</sub> plume, Geological Society, London, Petroleum Geology Conference series, 7, 1171–1182.
- Dvorkin, J., and Nur, A. (1996). Elasticity of high-porosity sandstones: Theory for two North Sea data sets. *Geophysics* 61, 890–893.
- Evans, B. J. (1997). A Handbook for Seismic Data Acquisition in Exploration, Geophysical Monograph Series, Society of Exploration Geophysicists, ISBN (print): 978-1-56080-041-5, ISBN (online): 978-1-56080-186-3.
- Ferguson, R.J., and Margrave, G.F. (2005). Planned seismic imaging using explicit one-way operators. *Geophysics* 70, 101–109.
- Gassmann, F. (1951). Über die Elastizität poröser Medien. *Vierteljahrsschrift der Naturforschenden Gesellschaft Zurich* 96, 1–23.
- Hashin, Z., Shtrikman, S. (1963). A variational approach to the theory of the elastic behaviour of multiphase materials. *J. Mech. Phys. Solids* 11, 127–140.
- Hill, R. (1952). The Elastic Behaviour of a Crystalline Aggregate. *Proc. Phys. Soc. Sect. A* 65, 349–354.
- Kumar, D. (2006). A Tutorial on Gassmann Fluid Substitution : Formulation, Algorithm and Matlab Code. *Geohorizons* 4–12.
- Margrave, G.F. (2000). New seismic modelling facilities in Matlab. *CREWES Res. Rep.* 12, 1–45.
- Mavko, G., Mukerji, T., and Dvorkin, J. (2009). The Rock Physics Handbook: Tools for seismic analysis of porous media: Cambridge University Press.
- Mindlin, R.D. (1949). Compliance of elastic bodies in contact, *Trans. ASME* 71, A-259.
- Mondol, N.H., Jahren, J., Bjørlykke, K., and Brevik, I. (2008). Elastic properties of clay minerals. *Lead. Edge*, 27, 758.
- Murphy, W.F. (1982). Effects of microstructure and pore fluids on the acoustic properties of granular sedimentary materials. Stanford University.
- Roach, L.A.N., White, D.J., and Roberts, B. (2015). Assessment of 4D seismic repeatability and *Geophysics*. 80, WA1-WA13.
- SEP (2017). Stanford exploration project, Introduction to seismic imaging, accessed September 26, 2017 at <http://sepwww.stanford.edu/data/media/public/sep/biondo/HTML/IntroRef.html>
- Williams, M.D., Vermuel, V.R., Oostrom, M., Porse, S.L., Thorne, P.D., Szecsody, J.E., Horner, J.A., and Gilmore, T.J. (2014). Design support of an above cap-rock early detection monitoring system using simulated leakage scenarios at the futureGen2.0 Site, in: *Energy Procedia*. pp. 4071–4082.

Yilmaz, O. (2001). Seismic Data Analysis: Processing, Inversion, and Interpretation of Seismic Data, in Investigations in Geophysics, Society of Exploration Geophysicists, doi:10.1190/1.9781560801580.

Zhu, X., and McMechan, G.A. (1990). Direct estimation of the bulk modulus of the frame in a fluid-saturated elastic medium by Biot Theory. SEG Tech. Progr. Expand. Abstr. 787–790.

## (2) GRAVITY MODELLING

### 2.1 Introduction

Gravity monitoring is one of the monitoring technologies available to evaluate and map the distribution of densities in the subsurface. This distribution of densities is reflected by changes in the local gravitational field. In the case of carbon sequestration, the injection of CO<sub>2</sub> into a reservoir will induce density changes by replacing the original fluid contained in the pores of the rock matrix by CO<sub>2</sub> (Figure 2.1). The CO<sub>2</sub> injection will produce a bulk density decrease because the density of the injected CO<sub>2</sub> is less than that of the brine. Further, any migration of the CO<sub>2</sub> underground will change the density distribution in the subsurface. The changes in density and the associated perturbations in the measured local gravitational field are referred to as anomalies. These gravity anomalies can be measured at the surface or in a borehole, using gravimeters.

To determine the density changes over time in the reservoir after the start of the injection, the total density of a given volume for a specific time step must be determined. This density is given as the *wet bulk density* and takes into account the density of the solid matrix, the brine and CO<sub>2</sub> in the pore space:

$$D_{wet\ bulk} = (1 - \phi)D_{rock} + S_w\phi D_w + S_{CO_2}\phi D_{CO_2}$$

where:  $S_w + S_{CO_2} = 1$  and,

$D_{wet\ bulk}$  = wet bulk density

$D_{rock}$  = rock matrix density

$D_w$  = brine density

$D_{CO_2}$  = CO<sub>2</sub> density

$\phi$  = porosity

$S_w$  = brine saturation

$S_{CO_2}$  = CO<sub>2</sub> saturation (any phase)

The form and the behavior of CO<sub>2</sub> depend of the conditions i.e., temperature and pressure, in the subsurface, as illustrated in the phase diagram in Figure 2.2. This means for example that under supercritical conditions, obtained at depths greater than 800 m, CO<sub>2</sub> takes a much smaller volume than a gas and is denser. On the other hand, if a migration of CO<sub>2</sub> occurs toward the surface, and the CO<sub>2</sub> undergoes a phase transition from supercritical to gas, the volume of CO<sub>2</sub>

could be much larger, and have also a lower density than displaced fluids. The gravity signal is directly proportional to changes in bulk density.

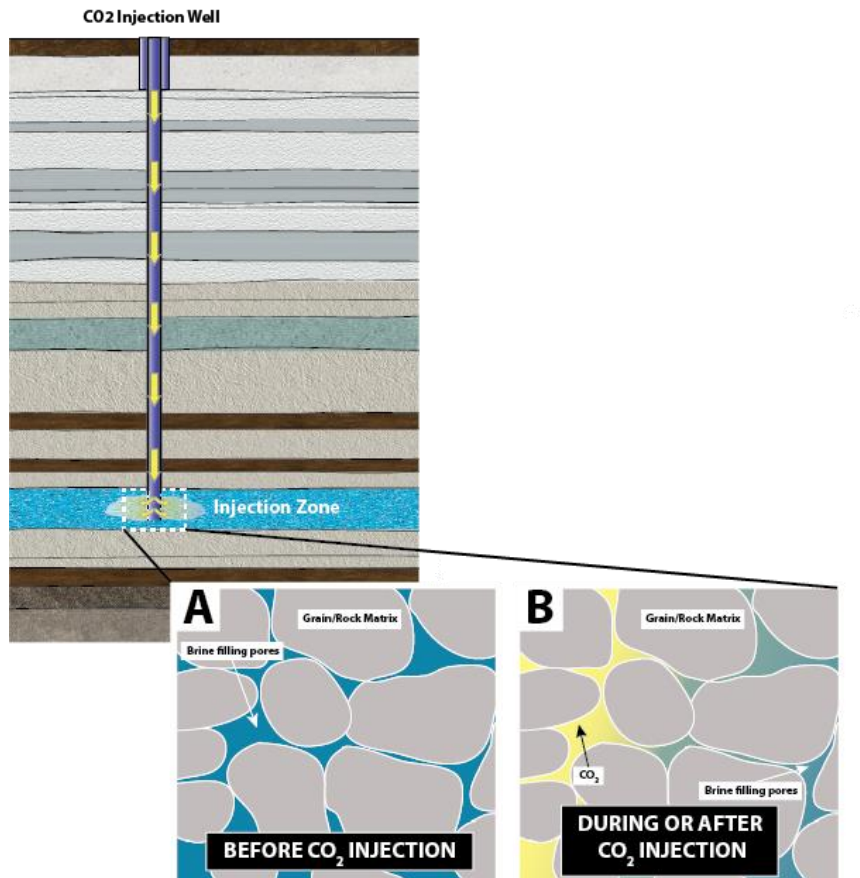


**Figure 2.1:** Schematic illustrating how brine is replaced by CO<sub>2</sub>. (A) Before injection, the pores are filled with brine. (B) During or after injection, the pores are filled with CO<sub>2</sub> leading to a change in bulk density.

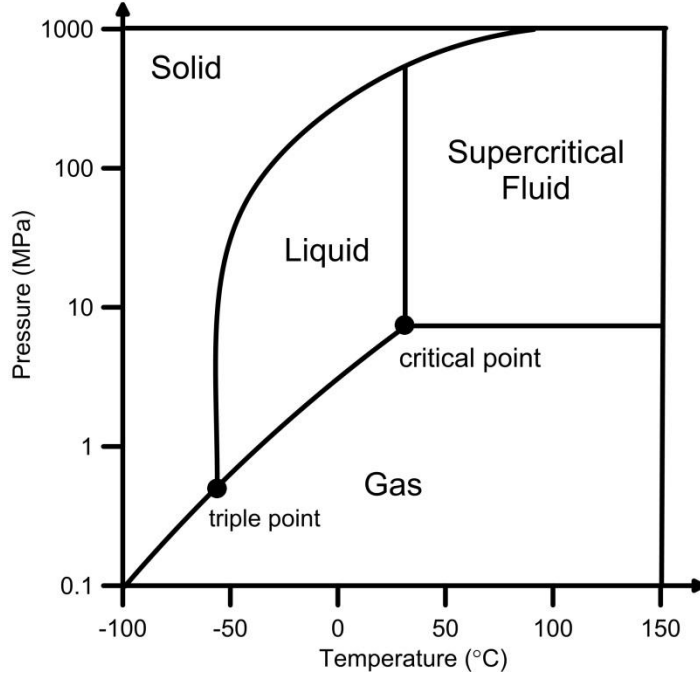


**Figure 2.2:** CO<sub>2</sub> phase diagram.

## 2.2 Gravity Forward Modeling

Synthetic multiphase flow simulations (e.g., Kimberlina 1.1, Kimberlina 2) will be converted to density models, and forward modeling will be carried out to calculate resulting gravity anomalies. The calculations will be done for various scenarios (e.g., no leakage, fault with permeability changes, wellbore leakage) using both surface and borehole sensor locations. The workflow of gravity modeling and analysis is presented in Figure 2.7 and consists of three main steps.

### Step 1: From Multiphase Flow Simulator Output to GRAV3D Input

The program GRAV3D v5.0 (University of British Columbia, Canada) will be used to conduct the gravity modelling. The program calculates the vertical component of the gravity response due to a 3D volume of density contrast. The density model is specified in the mesh of rectangular cells, each with a constant value of density contrast.

The output file formats of multiphase flow simulators (e.g., TOUGH2, STOMP) may differ, and therefore additional preprocessing steps might be required in order to be compatible with GRAV3D required inputs (examples of STOMP outputs are provided in Figures 2.3 and 2.4). Density calculations are done for each cell (volume) for each time step. The required parameters are: (a) grid with nodes coordinates, and (b) at each grid node and for each time step: either D<sub>wet\_bulk</sub> or D<sub>rock</sub>, D<sub>w</sub>, D<sub>CO<sub>2</sub></sub>, ϕ, S<sub>w</sub>, and S<sub>CO<sub>2</sub></sub>

Additional information regarding the injection operations, or the geological setting is:

- Injection point(s) or injection interval(s): x, y, z / x, y, zmin-zmax
- mass conservation equation used in the multiphase flow simulator to compute density (if any)
- General information regarding the geometry of the model such as presence and location of faults and location of monitoring points

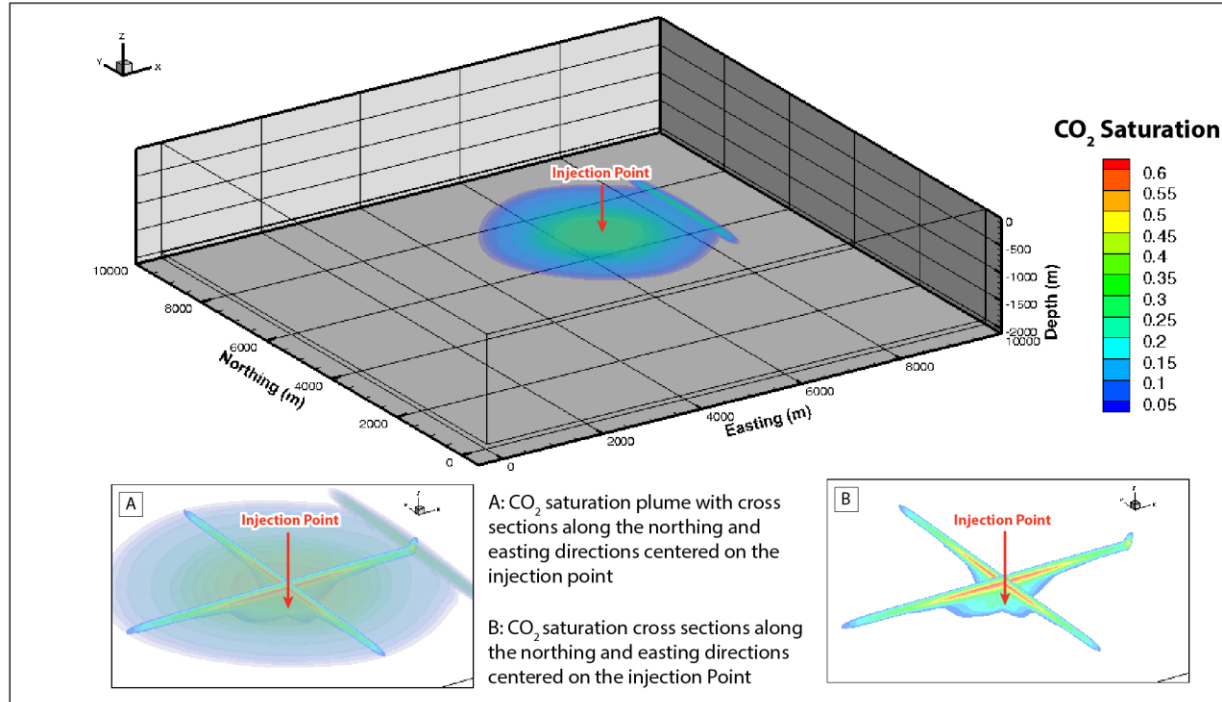


**Figure 2.3:** Example of output from STOMP multiphase flow simulator showing the CO<sub>2</sub> saturation at the end of the injection.

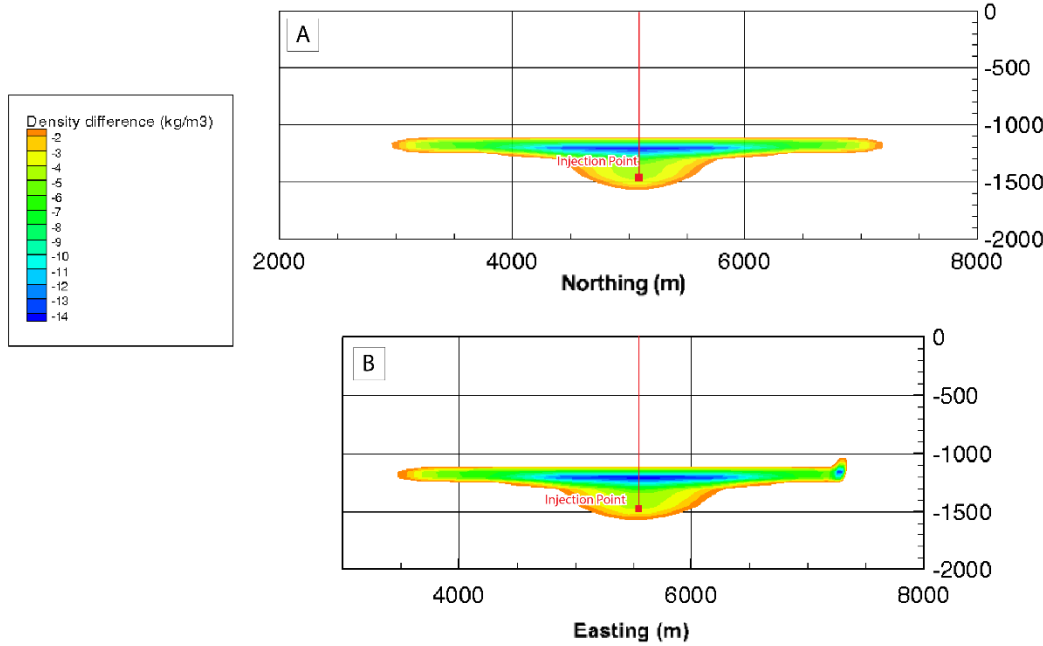


**Figure 2.4:** Example of density difference between the start and the end of CO<sub>2</sub> injection centered on the injection point along the easting (A), and northing (B) directions and computed from STOMP output files.

## Step 2: Model Conversion

### Output from STOMP multiphase flow simulator

STOMP output files provide the *wet bulk density* for any given point. A procedure has been written to convert the STOMP output files in a mesh that is directly readable by GRAV3D. The density distribution prior to injection (background) is subtracted from the post-injection distribution or from any desired time step. Then a MATLAB routine converts this file into the two input files required by GRAV3D: a regular mesh file and a density model file (Figure 2.5). This chain allows the user to directly compute the gravity anomalies linked to any distribution of densities generated by STOMP (Appriou et al., 2016).

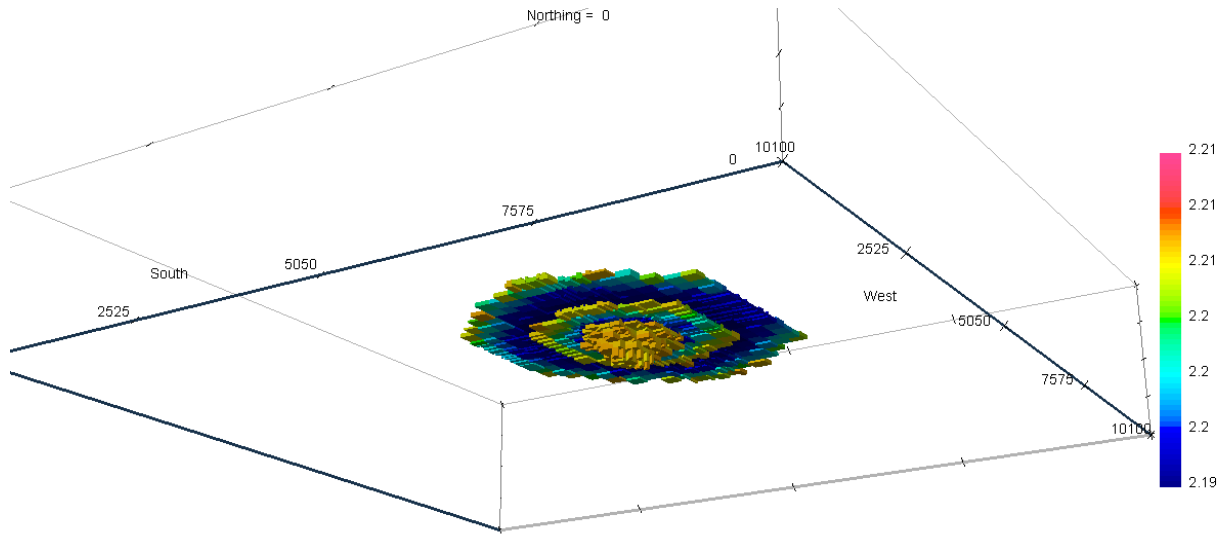


**Figure 2.5:** Density anomaly associated with a CO<sub>2</sub> plume after 30 years of injection

#### Output from TOUGH2 multiphase flow simulator:

Brine and CO<sub>2</sub> saturations and porosity are provided in the TOUGH2 output files. The density of brine and CO<sub>2</sub> are calculated using FORTRAN code for pressure and temperature values at each location. The output is an x, y, z, density file and the density distribution difference from any desired time step can be calculated. As for the STOMP case, then the Matlab subroutine converts this file into the two input files required by GRAV3D: a regular mesh file and a density model file.

#### Output from other multiphase flow simulator

If any additional multiphase flow simulator should be used to perform gravity forward modelling, similar steps, specific to the output formats of the simulator should be implemented in order to compute the required input files that would be used in GRAV3D.

### **Step 3 Forward Modeling**

The files obtained in step 2 are then uploaded in GRAV3D, and the gravity anomalies can be computed based on the distribution of density between two time steps. Surface and borehole gravity anomalies due to the CO<sub>2</sub> plume after 30 years of injection are shown in Figure 2.6.

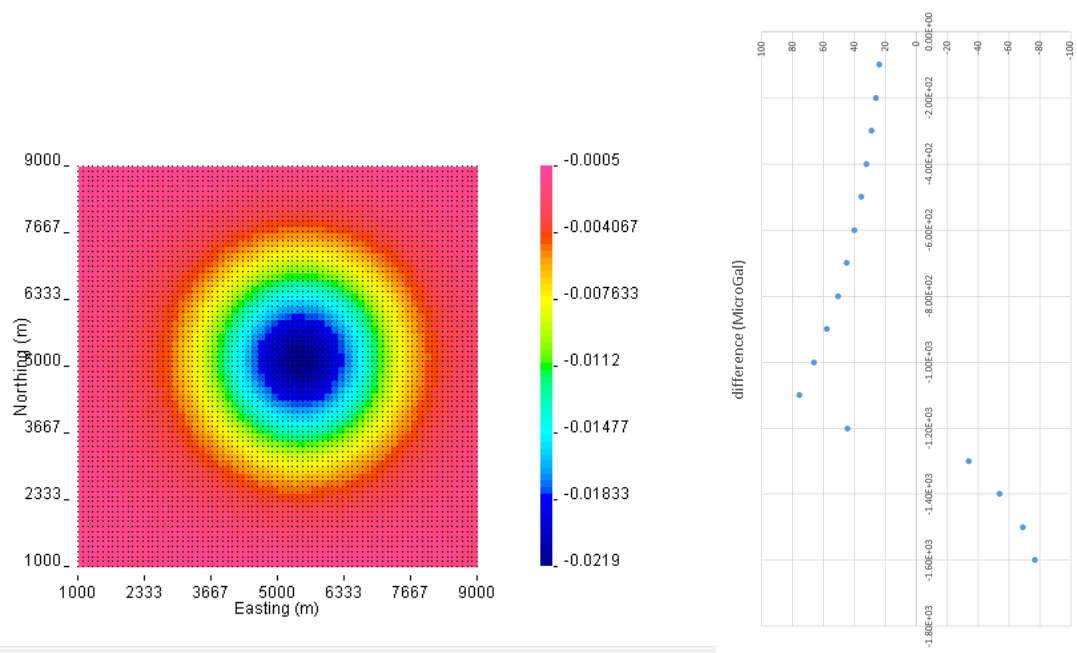


**Figure 2.6:** Surface gravity anomaly associated with the CO<sub>2</sub> plume after 30 years of injection (left) and borehole gravity anomaly associated with the CO<sub>2</sub> plume after 30 years of injection (right) computed in GRAV3D.

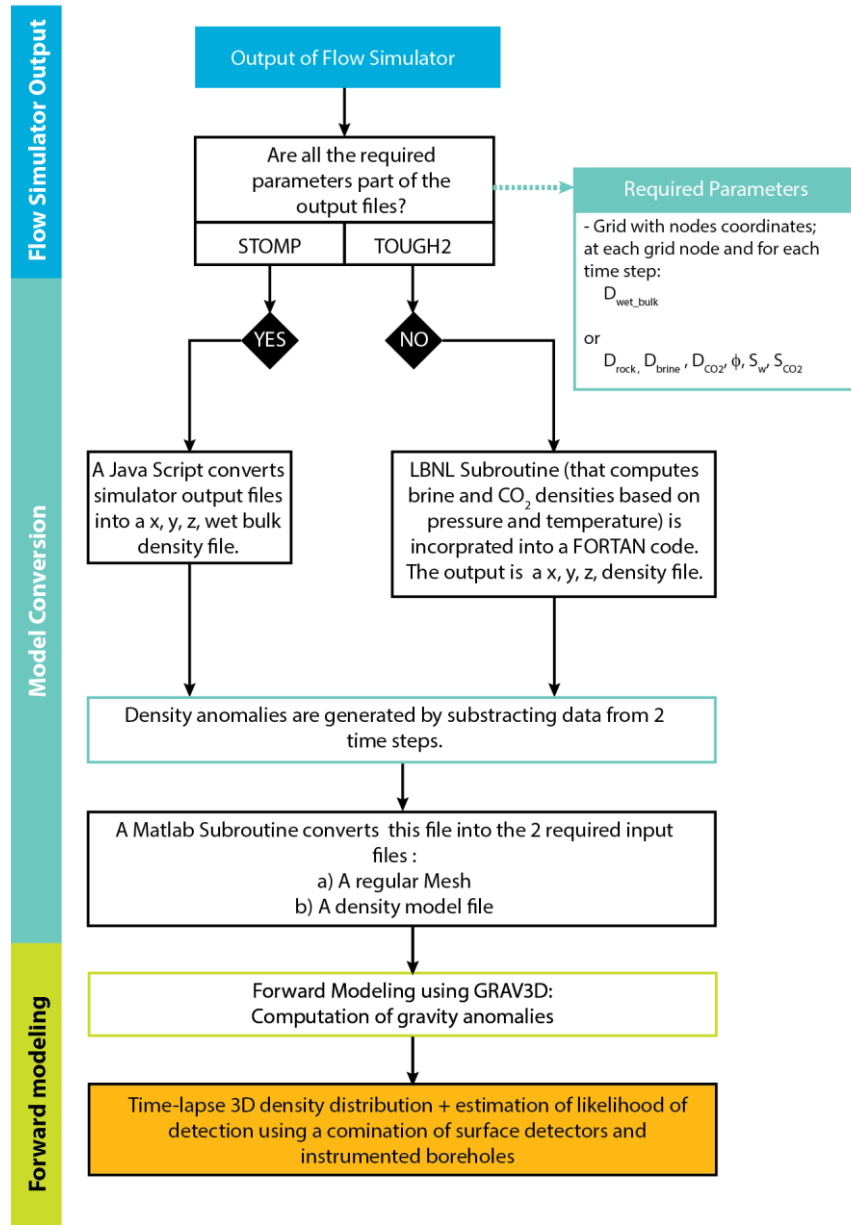


**Figure 2.7:** Workflow of forward gravity modeling and analysis.

### 2.3 References

Appriou D., A.H. Bonneville, B.N. Nguyen, and D.H. Bacon (2016). Evaluation of Time-Lapse Gravity Monitoring on a Faulted Carbon Sequestration Reservoir. Report. PNNL-25660, Pacific Northwest National Laboratory, Richland, WA.

## (3) ELECTRICAL AND ELECTROMAGNETIC METHODS

### 3.1 Introduction

Electrical and electromagnetic (EM) techniques measure electric (E) and magnetic (B or H) fields caused by currents that are injected into the ground by contacting electrodes or a time-varying magnetic field induced to flow into the ground by inductive sources. Electrical techniques, also called resistivity techniques, use only current and voltage measurements at frequencies low enough at which EM induction effects are negligible. Electrical Resistance Tomography (ERT) is one of them and it is described in Section 3.4. EM techniques require frequency-dependent sources to induce currents in the ground. Magnetic fields are produced from currents created from both types of sources. When the earth's natural electromagnetic fields are used as a source the technique is called magnetotellurics (MT) (see Section 3.6). The basic concept in all these techniques is to measure these electric and magnetic fields and to infer from these measurements the configuration and amplitudes of the current in the subsurface and hence the distribution of electrical resistivity.

Injected CO<sub>2</sub> is expected to form plumes of a finite size and change the subsurface resistivity resulting in a resistivity contrast with the enclosing formation. The goal of the survey is to identify a local variation in resistivity relative to the background geology. The changes in resistivity and the associated perturbations in the measured electric and magnetic fields are referred to as anomalies. The process of continuously measuring field variations due to the anomalies is referred to as monitoring.

The form and behavior of CO<sub>2</sub> depend on temperature and pressure. CO<sub>2</sub> behaves as a gas in air at standard pressure and temperature, as a solid (called dry ice) when frozen, or as a supercritical fluid at temperatures and pressures at or above the critical point (temperature of 31°C and pressure of 7.4 MPa) (Figure 3.1). Under supercritical conditions, which appear at depths greater than 800 m, CO<sub>2</sub> takes a much smaller volume than in the gas phase. The resistivity of CO<sub>2</sub> is high, similar to gas or air, independent of its state. Brine-bearing formations that are below and hydrologically separated from drinking water reservoirs have been widely recognized as having high potential for geologic CO<sub>2</sub> sequestration. The resistivity of brine depends on the amount of total dissolved solids (TDS), but in general is low (TDS = 10,000 ppm and up; parts per million; 1 ppm = 1 mg of salt in 1 liter of water). The relationship between fluid resistivity ( $\rho_w$ ) and TDS and temperature is shown in Figure 3.2.

The electrical resistivity of the subsurface is highly sensitive to changes in key formation properties such as porosity, pore fluid resistivity, and fluid saturation. A wide range of empirical relations exists for linking formation and electrical properties. Commonly used is Archie's Law (Archie, 1942), which describes the electrical resistivity ( $\rho_b$ ) of sedimentary rocks as a function of water saturation ( $S_w$ ), porosity ( $\phi$ ), and pore fluid resistivity ( $\rho_w$ ),

$$\rho_b = a \phi^{-m} \frac{\rho_w}{S_w^n}$$

where  $a$  is tortuosity, and  $m$  and  $n$  are constants with  $1.8 < m < 2$  and  $n \geq 2$ .

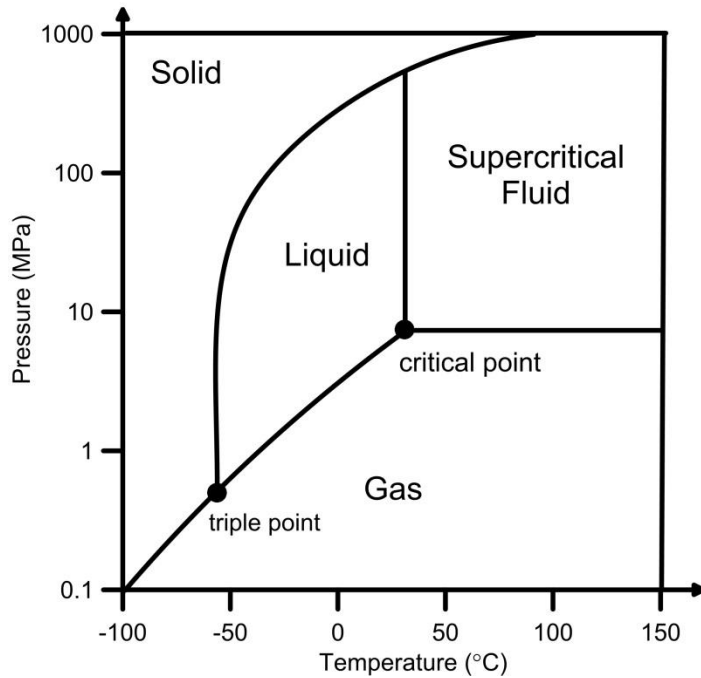


**Figure 3.1.** CO<sub>2</sub> phase diagram

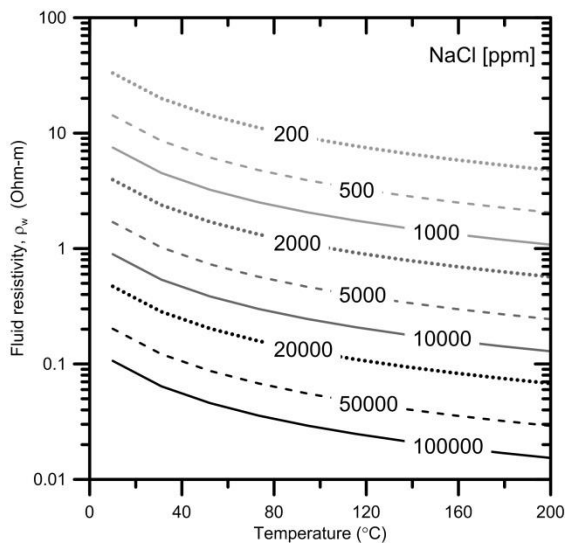


**Figure 3.2.** Fluid resistivity as a function of NaCl concentration and temperature.

When CO<sub>2</sub> is injected into a formation originally filled with brine, replacing brine with CO<sub>2</sub> results in a CO<sub>2</sub> saturation

$$S_{CO_2} = 1 - S_w = 1 - \left( \frac{a \rho_w}{\varphi^m \rho_b} \right)^{-n}$$

Figure 3.3 shows the rock bulk resistivity ( $\rho_b$ ) as a function of CO<sub>2</sub> saturation ( $S_{CO_2}$ ) for the formation with brine resistivity of 0.3 Ohm-m and 25% porosity. The replacement of highly conductive (low resistivity) saline fluids with resistive CO<sub>2</sub> results in resistivity increase in the storage reservoir. When CO<sub>2</sub> is present at shallow depths, dissolution of CO<sub>2</sub> causes increase in TDS and results in resistivity decrease.

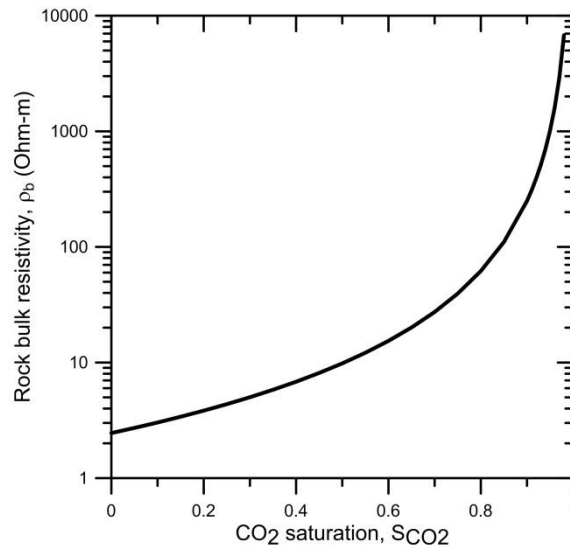


**Figure 3.3.** Rock bulk resistivity ( $\rho_b$ ) as a function of CO<sub>2</sub> saturation ( $S_{CO_2}$ ). Pore fluid resistivity is 0.3 Ohm-m, porosity is 35%,  $a = 1$ ,  $m = 2$ , and  $n = 2$ .

Electrical resistivity can be used to determine CO<sub>2</sub> saturation:

$$S_{CO_2} = 1 - S_w = 1 - \frac{a \rho_w}{\varphi^m \rho_b}.$$

Complex mineral composition may affect bulk rock parameters, and estimates of CO<sub>2</sub> saturations using Archie's equation might not be accurate. In such situations, another useful and simple relationship between resistivity and brine saturation, the resistivity index (Gueguen, 1994), can be used:

$$RI = \frac{\rho}{\rho_0} = (S_w)^{-n},$$

where  $\rho$  is the resistivity of the rock partially saturated with brine,  $\rho_0$  is the resistivity of fully saturated rock with brine, and  $n$  is the saturation exponent. Again, in the case of CO<sub>2</sub> injection, it is possible to estimate CO<sub>2</sub> saturation from the initial resistivity of the fully saturated rock with brine and partial brine saturation during CO<sub>2</sub> injection using:

$$S_{CO_2} = 1 - \left( \frac{1}{RI} \right)^{1/n}.$$

When a formation contains a substantial amount of clay, an additional parameter – the ratio of volume of sand to volume of clay – is necessary (e.g., Nakatsuka et al., 2010).

In resistivity techniques, the resistivity of the ground is measured by injecting electrical currents into the ground and measuring the resulting potential differences. The electrodes can be on the surface as well as in boreholes. Figure 4 illustrates a decrease in the response with increasing distance between the target and where the measurements are made.

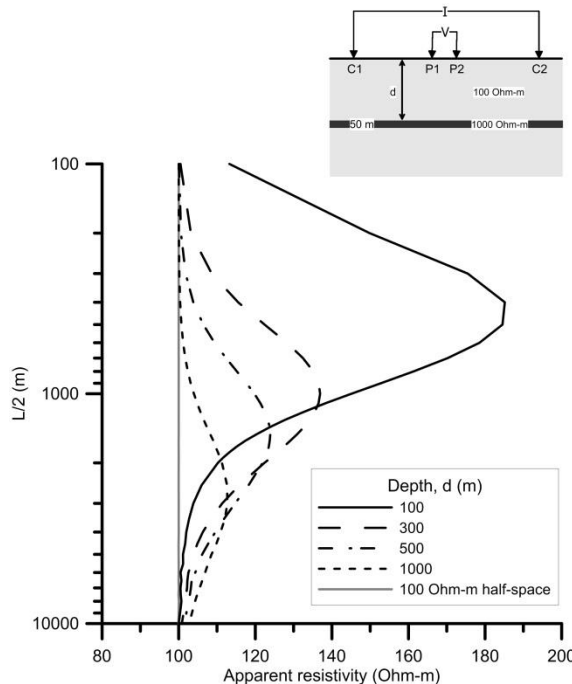


**Figure 3.4.** Apparent resistivity response of 1000 Ohm-m and 50 m thick layer in a 100 Ohm-m half-space as a function of layer depth.

Figure 3.5 illustrates that resistivity techniques are much more sensitive to low resistivities (conductive targets).

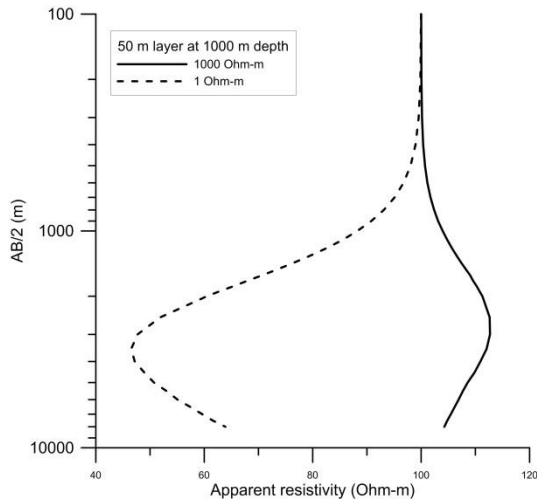


**Figure 3.5.** Apparent resistivity response of deep conductive and resistive layers.

### 3.2 EM techniques for resistive targets

An example of a deep resistive target is an electrical resistivity model derived from Kimberlina 1 reservoir model. The model is  $\sim 15 \times 10$  km in x and y directions respectively and 5 km in the vertical direction. A vertical cross-section through the model along the x-direction (Easting) at the y-coordinate of the injection well is shown in Figure 3.6. The top of the reservoir near the fault is  $\sim 1$  km, and there is no CO<sub>2</sub> present outside of the reservoir, therefore upper 1 km is not shown. Figure 3.6 shows distribution of porosity, and CO<sub>2</sub> saturations at years 49 and 175 since the start of injection. The injection well is located at Easting = 297,000 m. The CO<sub>2</sub> was injected for 50 years.

The baseline electrical resistivity model before CO<sub>2</sub> injection is estimated using an equation described below. Inside the reservoir, the bulk resistivity is given as

$$\rho_b = a \cdot \phi^{-m} \cdot \rho_f, \text{ where } a=1, m=2, \text{ and } \rho_f \text{ is a pore fluid resistivity.}$$

It is assumed that the pore fluid resistivity ( $\rho_f$ ) linearly changes from 0.16 Ohm-m at 3 km in depth to 0.3 Ohm-m at 2 km. These limits are based on the salinity and temperature values shown in Figure 3.7. This linear relationship is used to determine a pore fluid resistivity inside the reservoir as a function of depth. The resistivity between the top of the reservoir and z=1 km is determined by sedimentary rock types of model cells: 8 Ohm-m is used for clay and 19 Ohm-m is used for sand. Resistivity values above z=1 km and below the bottom of reservoir are set to 19 Ohm-m and 100 Ohm-m, respectively.

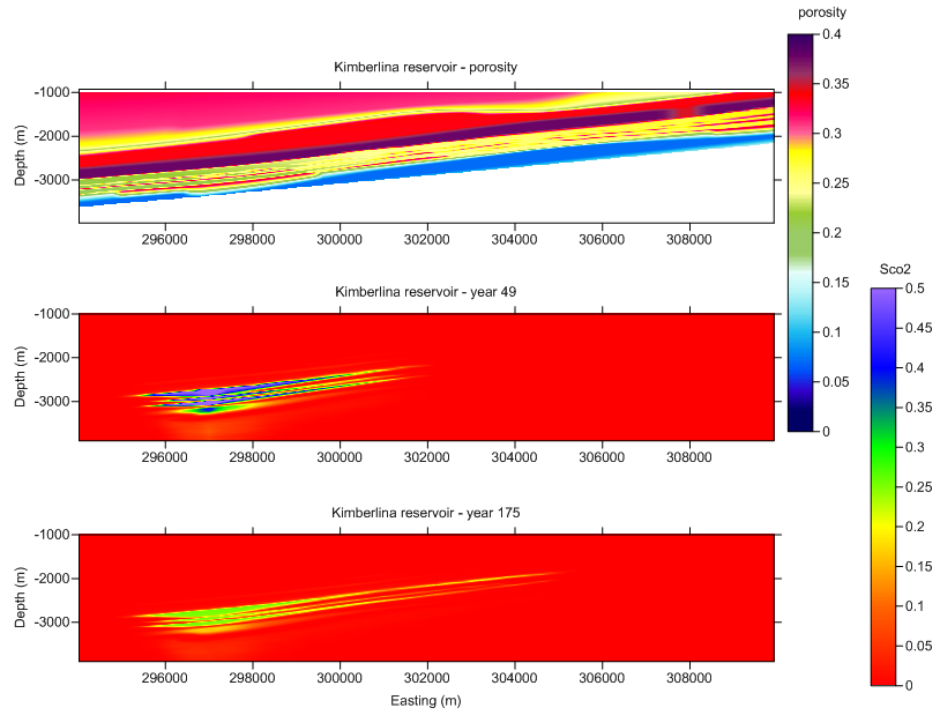


**Figure 3.6.** Kimberlina 1 reservoir porosity (upper panel) and CO<sub>2</sub> saturations at 49 and 175 years since the start of injection (bottom two panels).

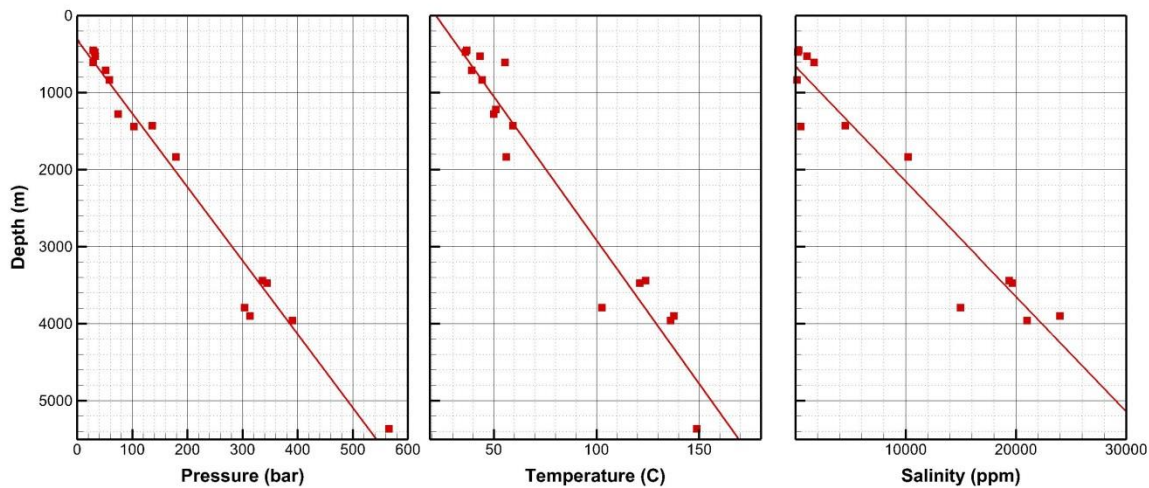


**Figure 3.7.** Kimberlina (a) pressure, (b) temperature, and (c) salinity profiles (solid lines) as a function of depth using available measurements (dots).

The injection of CO<sub>2</sub> increases the electrical resistivity inside the reservoir. In this example, we consider resistivity perturbations in the reservoir at two time intervals: 49 years and 175 years.

To calculate the increased electrical resistivity, a reservoir cell with a non-zero CO<sub>2</sub> saturation value is updated using

$$\rho' = \frac{\rho}{(1-S_{\text{CO}_2})^m}, \text{ where } m=2 \text{ and } S_{\text{CO}_2} \text{ is a CO}_2 \text{ saturation at a given cell at a given year.}$$

Figure 3.8 shows resistivity models for the start of the injection, and at 49 and 175 years since the start of CO<sub>2</sub> injection.

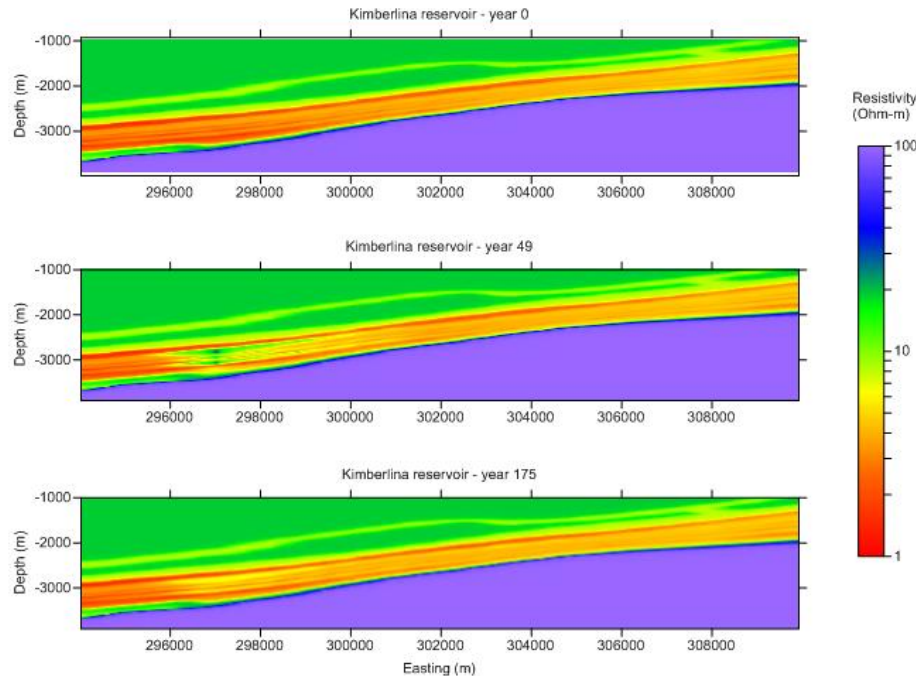


**Figure 3.8.** Kimberlina 1 resistivity models: background (upper), 49 year (middle), and 175 year (bottom).

To evaluate the sensitivity of a controlled-source electromagnetic (CSEM) method to the CO<sub>2</sub> plume (resistive target) using surface and borehole transmitters and surface receivers, CSEM responses of these three models were simulated using EMGEO, a 3D finite-difference electromagnetic modeling and imaging algorithm (Commer and Newman, 2008). The fine vertical cells faithfully delineate details of reservoir structures and resistivity perturbation due to CO<sub>2</sub> injection. However, the direct use of the fine grids is computationally too expensive and unnecessary. In order to reduce the computational cost without affecting the solution accuracy, EMGEO employs a material averaging scheme based on a parallel-circuit integro-interpolation method (Moskow et al., 1999; Commer and Newman, 2008). The method maps the original dense grid models into coarse grids called simulation/computation grids. The mapping algorithm

has proven effective for modeling resistivity contrasts on the order of  $10^3$  or less (Hoversten et al., 2015). The simulation grids are designed based on a wave length for accurate solutions and are surrounded with about three skin-depth-thick buffer layers to attenuate the unwanted reflections of the electric fields from the boundaries. CSEM is one of EM techniques that is using a finite length transmitter and electric dipoles as receivers. The responses are calculated for each transmitter-receiver configuration at a specific frequency. Figure 3.9 is an example of 1D EM response for a borehole-to-surface configuration: amplitude, phase, real and imaginary parts of the electric field are plotted as a function of distance from the borehole for two times. The changes are relatively small. In order to identify a subsurface structure that produces signals measured by the array of receivers the use of an inversion algorithm is required.

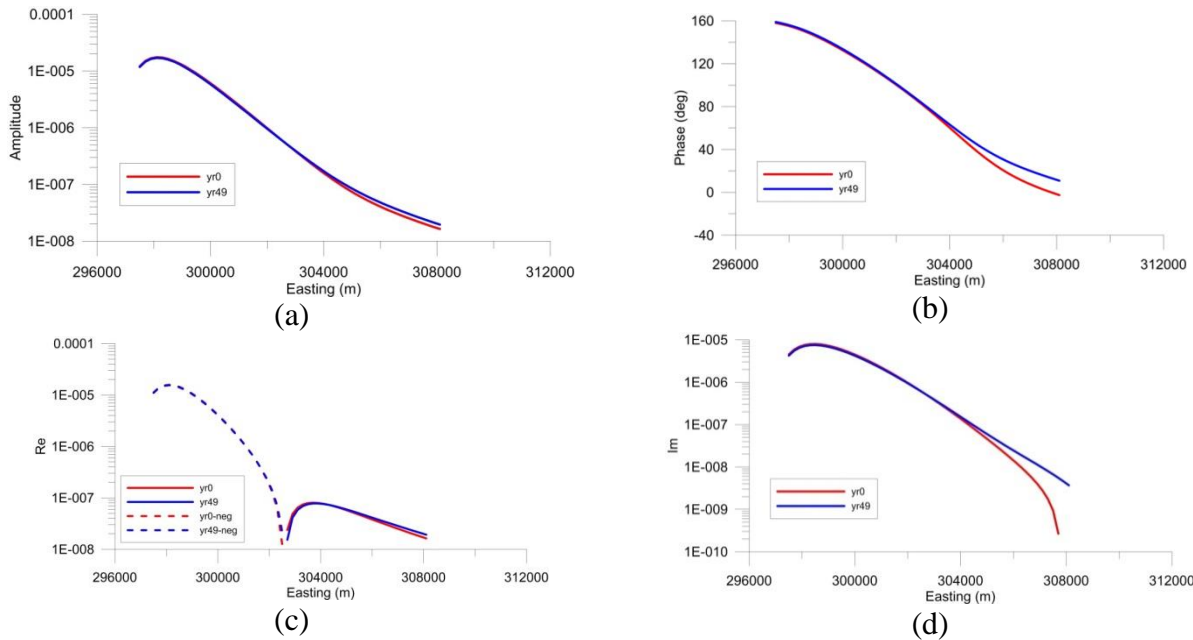


**Figure 3.9.** Example of 1D EM responses: (a) amplitude, (b) phase, (c) real and (d) imaginary part of the electric field as a function of distance for a borehole-to-surface electrode configuration. Red is the background response, blue is the response at 49 years.

### 3.3 EM techniques for conductive targets

An example of a shallow conductive target is an electrical resistivity model derived from High Plains aquifer impact model (simulation 0040 is used as an example).

A horizontal slice through the TDS plume at the time when the anomaly was the largest is shown in Figure 3.10. The background response is <600 ppm (not shown).

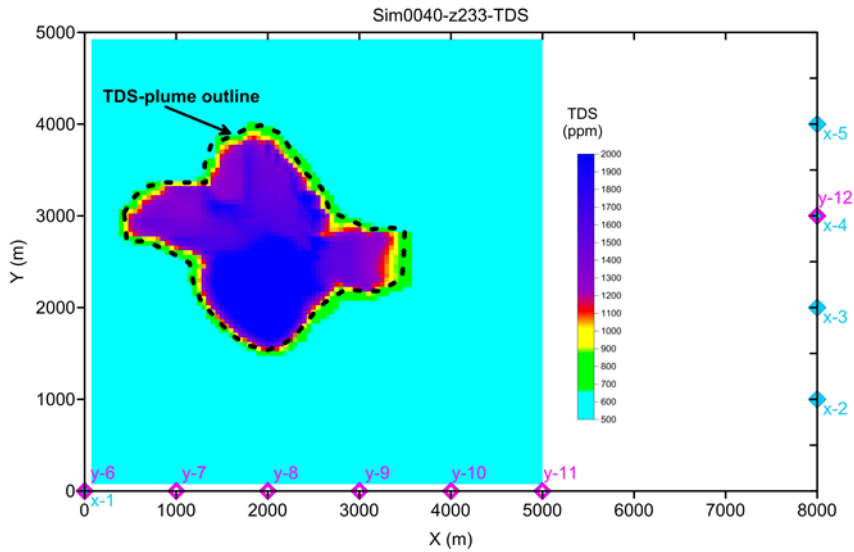


**Figure 3.10.** TDS anomaly as a function of x and y at the depth of 233 m.

The resistivity model was constructed using 3D distributions of sand, clay, TDS values, and following parameters and formulas:

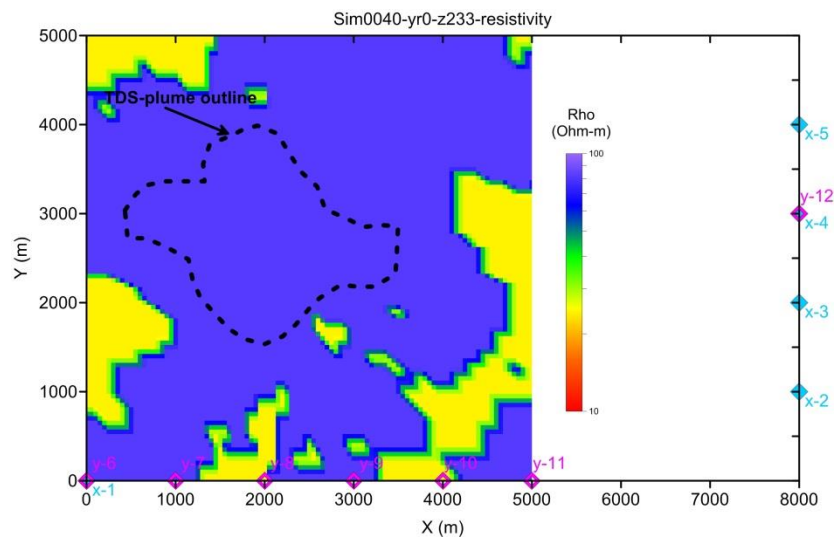
The fluid resistivity was calculated using:  $\rho_f = \frac{\rho_{18C}}{1 + \alpha(t - 18)}$ , where  $\rho_{18C} = 3549 / c^{0.924}$ ,  $c$  is the TDS value in ppm, and alpha = 0.025.

The bulk resistivity was calculated using Archie's law:

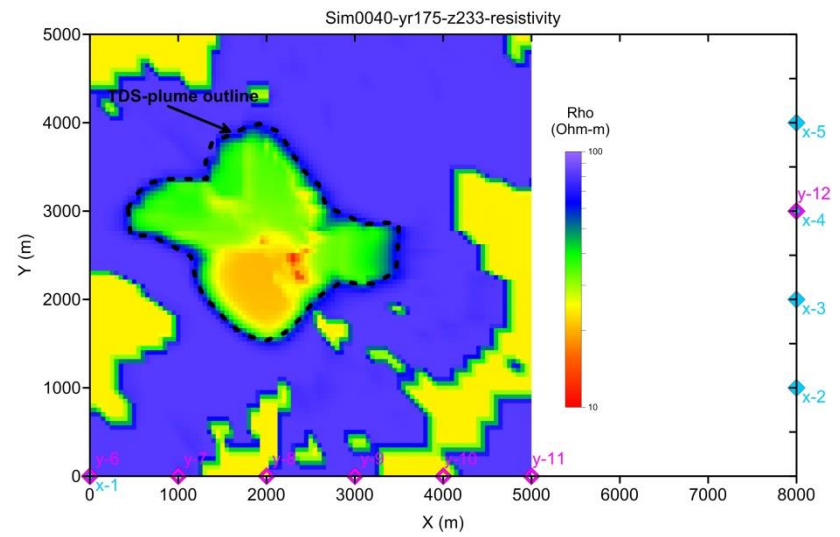
$$\rho_b = a \cdot \phi^{-m} \cdot \rho_f, \text{ where } a=1, \rho_f \text{ is a pore fluid resistivity}$$

Values of porosity and m varied depending if the model cell contained sand or clay. The porosity and m for sand were 0.35 and 2, respectively, while the porosity and m for clay were 0.45 and 1.1, respectively.

Figure 3.11 shows that the models were accurately converted to resistivity models and the TDS changes up to 2000 ppm correspond to 50-80% decrease in bulk resistivity.



(a)



(b)

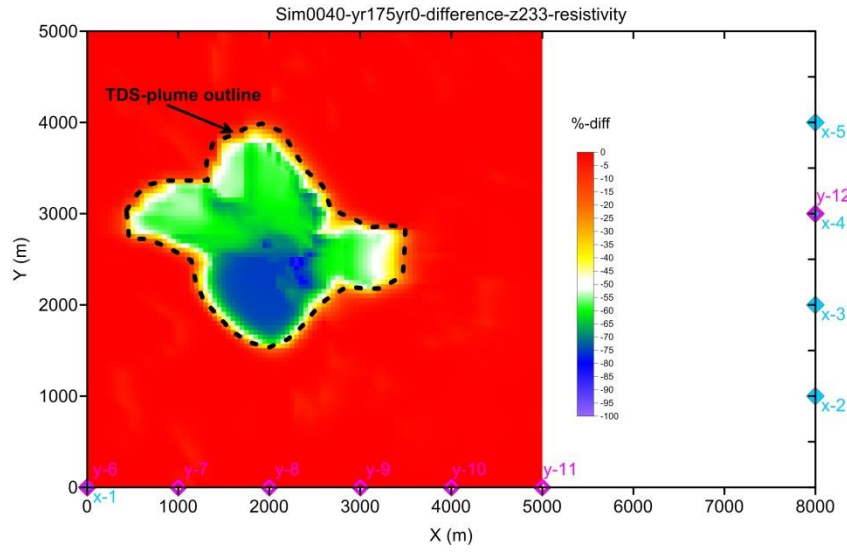


**Figure 3.11.** Resistivity model of (a) background, (b) TDS anomaly from Figure 3.10, and (c) difference between (a) and (b).

Figure 3.12 shows a response for a CSEM configuration using an electric field dipole as a transmitter and grid of electric dipole receivers. 10-20% difference in the imaginary component of the electric field outlines the location and the lateral extent of the TDS plume very well. In order to find out the depth of the plume that produces these responses an inversion algorithm is required.

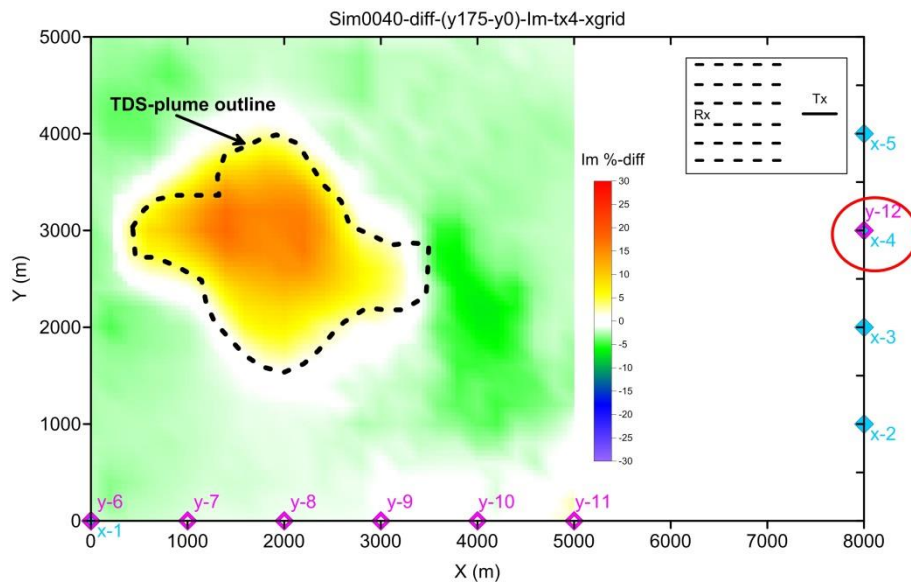


**Figure 3.12.** Percent difference in the imaginary component of the surface electric field for one transmitter and a grid of receivers for the models shown in Figure 3.11.

### 3.4 Electrical Resistance Tomography (ERT)

Electrical resistance tomography (ERT) is an indirect method for visualizing the movement of fluids in porous media that requires the use of inversion algorithms that convert raw measurements of electrical resistance to a tomographic image (resistivity or concentration) of a fluid plume. In an ERT survey, tens or hundreds of electrodes are deployed either in monitoring wells or on the ground surface. To take an ERT measurement, a known electric current is injected into the earth through a pair of electrodes and the induced electric potential difference is measured by another pair of electrodes. An apparent resistivity value is calculated from the injected current, observed voltage and electrode locations. Hundreds or thousands of measurements can be obtained by various combinations of electrodes. To monitor a subsurface process such as a CO<sub>2</sub> leakage, a no-leak baseline data set is collected. Monitor data sets are collected at specific time intervals. The potential leakage may be detected by comparing the monitoring data with the baseline data.

### 3.5 Surface ERT for conductive targets

Geophysical models were created using simulated aquifer impact models based on a hypothetical, compartmentalized, CO<sub>2</sub> storage reservoir in the Vedder Formation in Kimberlina, Kern County in California's southern San Joaquin Basin (Buscheck et al., 2017). Figure 3.13 shows the reservoir and wellbore models. Brine and CO<sub>2</sub> leakage results in subsurface changes in pressure, CO<sub>2</sub> saturation and total dissolved solids (TDS). CO<sub>2</sub> buoyancy allows a significant fraction of leaked CO<sub>2</sub> to reach shallower permeable zones (Figure 3.14).

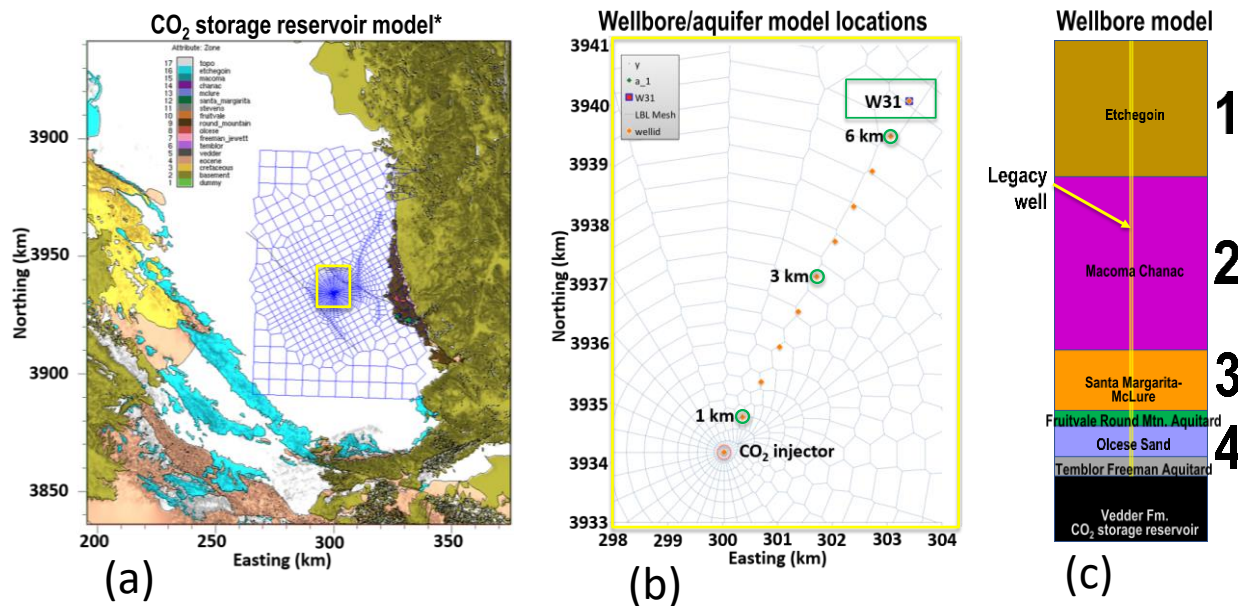


**Figure 3.13.** Site location with reservoir model mesh (a), well locations (b), and conceptual wellbore model (c).

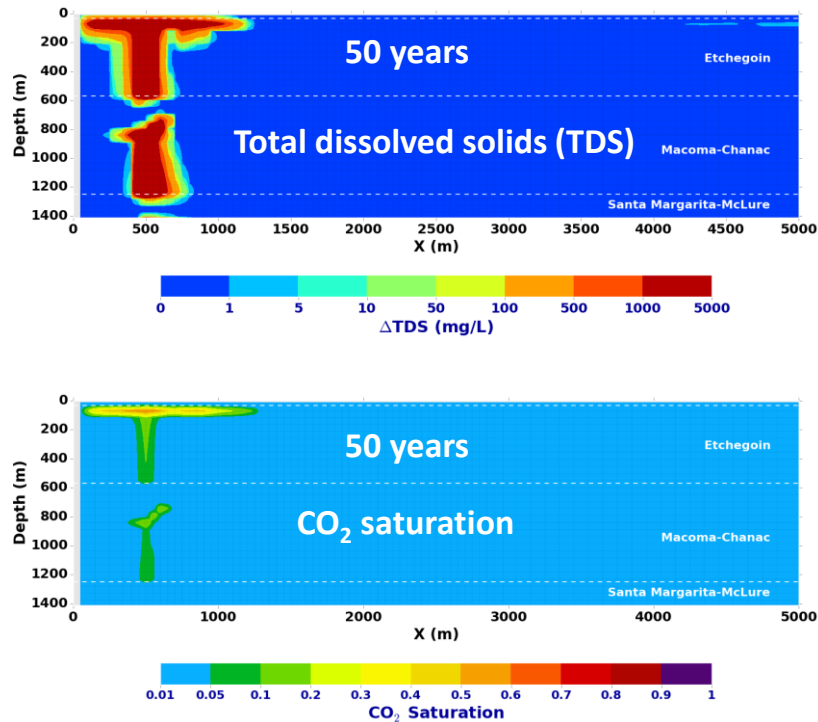


**Figure 3.14.** Contour plots of total dissolved solids (TDS) increase above background (top) and CO<sub>2</sub> saturation (bottom) are shown at 50 years for a leaking well 1 km from the CO<sub>2</sub> injector, the P90S50 wellbore case, a high groundwater gradient, high wellbore permeability, and two leaky aquifers.

Leakage of CO<sub>2</sub> and brine into groundwater changes the pore species concentrations (Na<sup>+</sup>, Cl<sup>-</sup>, HCO<sub>3</sub><sup>-</sup>, H<sup>+</sup>, Ca<sup>2+</sup>, CO<sub>2</sub> (gas) and CO<sub>2</sub> (aqueous)) and electrical conductivity (EC). The pore-fluid EC can be estimated directly from these ion concentrations (Visconti et al., 2010) or from TDS values found in the Kimberlina simulation data (Walton, 1989). The equation used to convert TDS to water EC is:

$$\text{TDS (mg/L)} = 8000 \text{ EC (S/m)}$$

The bulk formation conductivity (inverse of resistivity) was obtained through Archie's equation (Archie, 1942) with knowledge of the formation porosity and water or gas saturation.

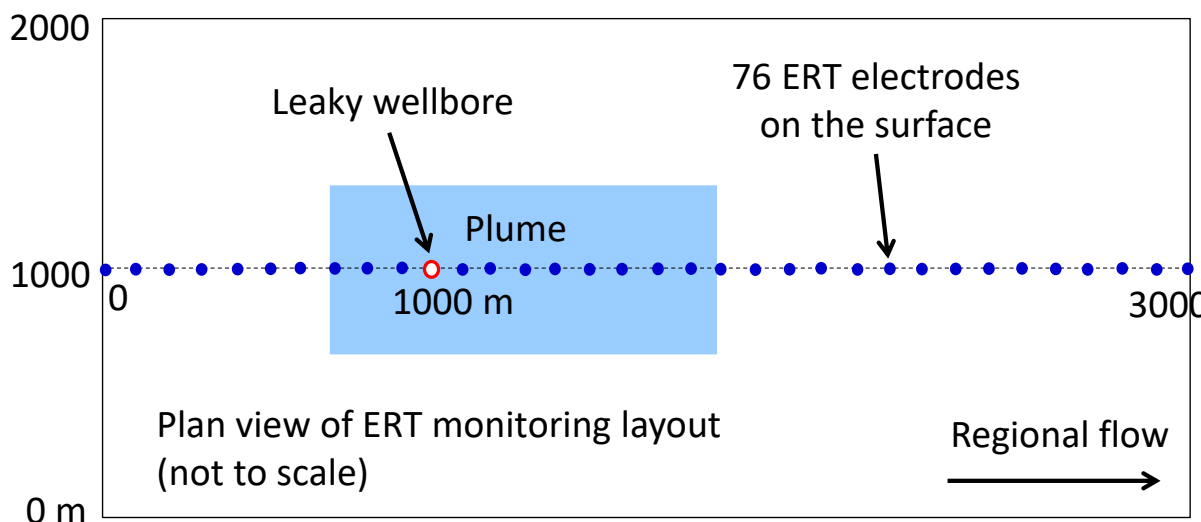
In this study, the TDS changes in 140 models were converted into subsurface electrical conductivity distributions at seven time steps: 0, 10, 20, 50, 100, 150 and 200 years, which resulted in 980 electrical conductivity models. A uniform constant porosity was set to 0.35. The simulated TDS changes were added to a three-layer baseline TDS model (Table 1).

**Table 1.** Pre-leak baseline TDS model and electrical resistivity models

Layer Number	Depth (m)	TDS (mg/L)	Resistivity (Ohm-m)
1	0-200	500	131
2	200-500	1,000	65
3	>500	2,000	33

In a shallow aquifer, dissolved CO<sub>2</sub> lowers fluid resistivity but gas-phase CO<sub>2</sub> increases formation resistivity. These two opposite effects cancel each other to certain extent, but dissolved CO<sub>2</sub> has a greater impact on formation resistivity, which results in overall decrease of formation resistivity (Yang et al., 2015).

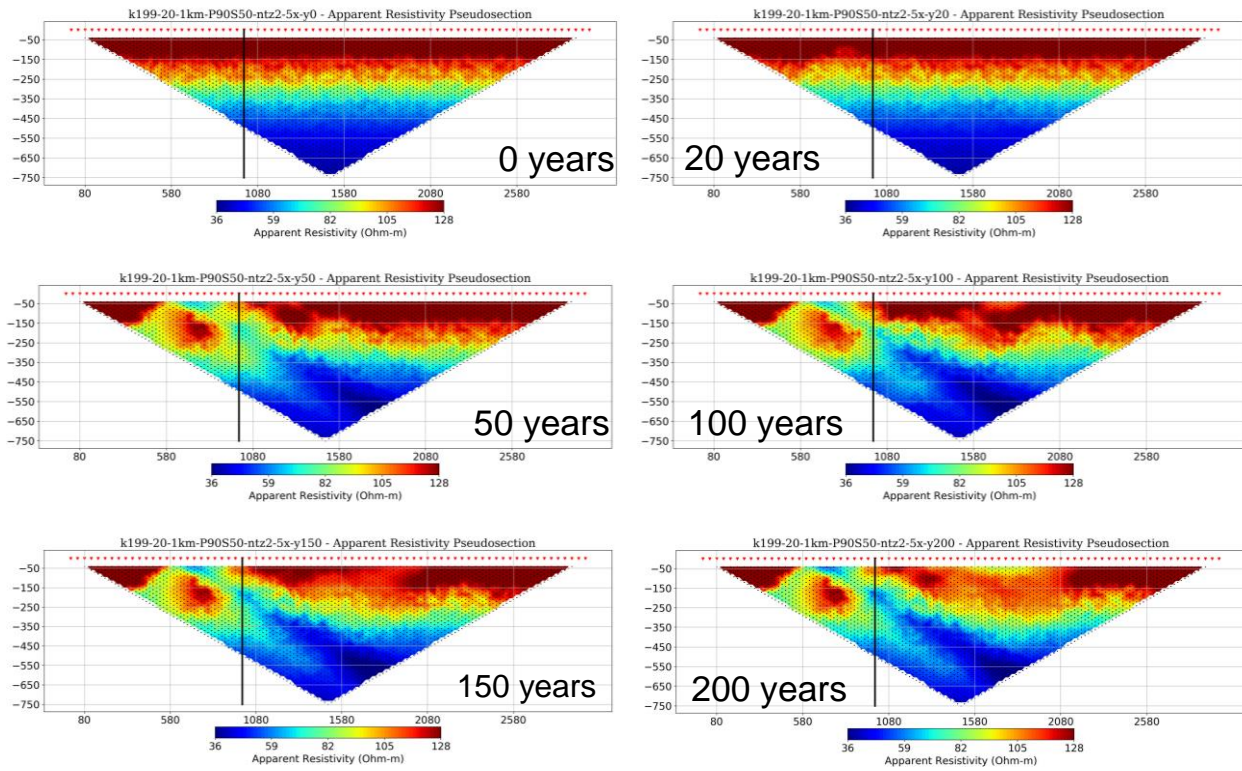
76 ERT electrodes were placed at 40-m spacing along the center line of likely leakage plumes (Figure 3.15). The 2-D ERT monitoring profile was 3000-m long, which gave an approximate depth of penetration of 600 m when the transmitter and receiver dipoles were on opposite ends of the profile. The regions near the two ends of the profile are poorly resolved. Therefore, the length of the profile is often much larger than the area of interest. The monitoring data were compared with the baseline data to estimate percent changes in apparent resistivity values.



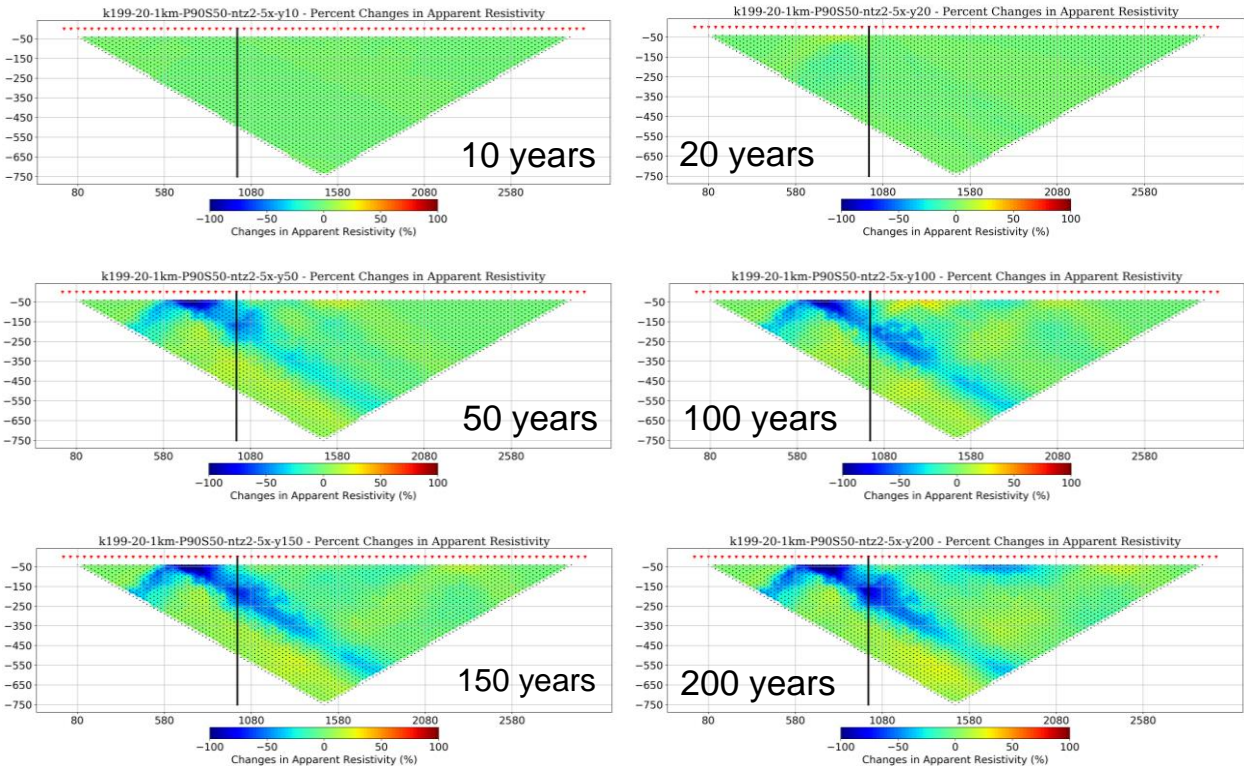
**Figure 3.15.** Layout of 76 ERT electrodes at 40-m spacing along the center line of a likely leakage plume.

Figure 3.16 shows the ERT apparent resistivity pseudosections at six time steps. The pre-leakage (0 years) baseline model is a three-layer resistivity model (Table 1). As the plume grows,

electrical resistivity decreases mostly due to elevated TDS from dissolved CO<sub>2</sub>. The maximum vertical depth on the pseudosection is set to 750 m due to the limited depth of penetration. Figure 3.17 was created by taking the percent difference between the monitoring and baseline data in Fig. 3.16. The percent changes in apparent resistivity illustrate clearly the effect of CO<sub>2</sub> plume on the ERT data. No ERT anomaly is observed at 20 years. From 50 years to 200 years, the ERT anomaly grows larger. Note, the pseudosection is not an actual depth section, and a ‘pant-leg’ pattern visible especially in Figure 3.17 is due to the data plotting convention. ERT inversion would be used to recover intrinsic subsurface resistivity changes and would be close to the TDS distribution similar to the one shown in Figure 3.14.



**Figure 3.16.** ERT apparent resistivity pseudosections at six time steps for a leaking well 1 km from the CO<sub>2</sub> injector, the P90S50 wellbore case, a high groundwater gradient, high wellbore permeability, and two leaky aquifers (Fig. 3.14). The vertical black line at 1000 m indicates the wellbore location.

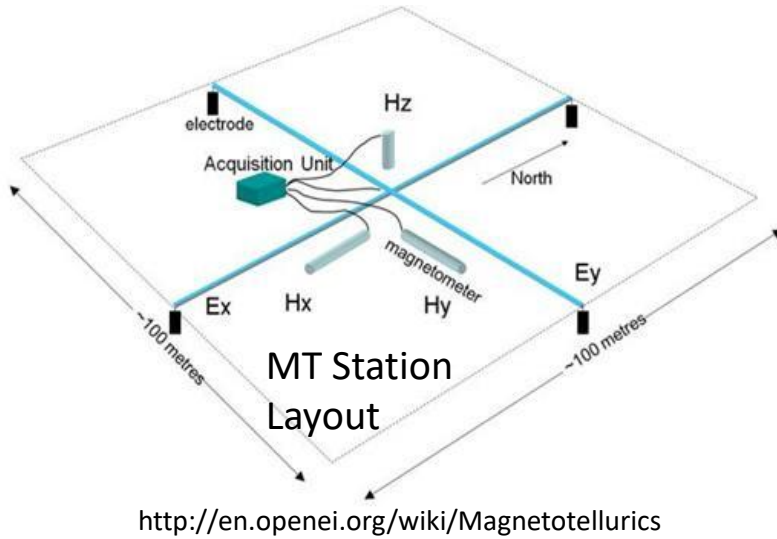


**Figure 3.17.** ERT pseudosections of percent change in apparent resistivity at six time steps.

### 3.6 Magnetotelluric method (MT)

The magnetotelluric (MT) method is a passive surface EM technique that uses the earth's natural EM fields to probe the electrical resistivity structure of the earth at depths of tens of meters to hundreds of kilometers (Chave and Jones, 2012; Simpson and Bahr, 2005). The natural EM source fields consist of (1) micro-pulsations (<1 Hz) due to the interaction of solar wind with the geomagnetic field; and (2) global lightning activities (>1 Hz). These large-scale source fields are treated as uniform plane waves propagating vertically into the earth. When the measurements are made in 1 Hz to 10 kHz frequency range, the method is referred to as audio-frequency or AMT. Advantages of AMT include rapid data collection and a large number of data stacks for noise reduction. A disadvantage is that AMT dead bands around 1 Hz, and 1 kHz to 5 kHz have an unstable energy source with diurnal and annual variation (Garcia and Jones, 2008; García and Jones, 2005; Iliceto and Santarato, 1999), which may compromise AMT data quality. To overcome this deficiency, researchers developed effective data acquisition and processing methods (Garcia and Jones, 2008; García and Jones, 2005). An alternative approach to improve the signal-to-noise ratio is to use an active source, and the technique is then called controlled source audio frequency MT (CSAMT) (Streich et al., 2010).

Time series of two electric field components ( $E_x$  and  $E_y$ ) and three magnetic field components ( $H_x$ ,  $H_y$ , and  $H_z$ ) are measured at a station (Figure 3.18).



[http://www.kmstechnologies.com/MT\\_survey\\_system.html](http://www.kmstechnologies.com/MT_survey_system.html)

**Figure 3.18.** The field setup of an MT station with two electric field dipoles ( $E_x$  and  $E_y$ ) and three orthogonal magnetic coils ( $H_x$ ,  $H_y$ , and  $H_z$ ). The lower image shows MT equipment with magnetometer coils (black long cylinders) and four electrodes (gray and yellow).

These electric and magnetic fields are then transformed into the frequency domain and related through the impedance tensor ( $Z$ ):

$$\begin{pmatrix} E_x \\ E_y \end{pmatrix} = \begin{pmatrix} Z_{xx} & Z_{xy} \\ Z_{yx} & Z_{yy} \end{pmatrix} \begin{pmatrix} H_x \\ H_y \end{pmatrix}$$

The EM fields are often decoupled into two independent modes. One mode has the electric field parallel to the strike of a structure, i.e., E-polarization or transverse electric (TE) mode, and another mode has the magnetic field parallel to the strike, i.e., B-polarization or transverse

magnetic (TM) mode. Apparent resistivity and phase for TE and TM modes are calculated for ease of data visualization. In the TE mode, the apparent resistivity ( $\rho_{xy}$ ) and phase ( $\varphi_{xy}$ ) are given by

$$\rho_{xy}(\omega) = \frac{1}{\mu_0 \omega} |Z_{xy}(\omega)|^2$$

$$\varphi_{xy}(\omega) = \tan^{-1} \left( \frac{\text{Im}\{Z_{xy}\}}{\text{Re}\{Z_{xy}\}} \right)$$

and in the TM mode:

$$\rho_{yx}(\omega) = \frac{1}{\mu_0 \omega} |Z_{yx}(\omega)|^2$$

$$\varphi_{yx}(\omega) = \tan^{-1} \left( \frac{\text{Im}\{Z_{yx}\}}{\text{Re}\{Z_{yx}\}} \right)$$

Both apparent resistivity and phase are functions of an angular frequency ( $\omega=2\pi f$ ), and  $\mu_0 = 4\pi \times 10^{-7}$  H/m is magnetic permeability in free space. For a uniform half space (1D), the apparent resistivity in both TE and TM modes is equal to the true resistivity of the earth with a phase of  $45^\circ$ , indicating that the electric field precedes the magnetic field by  $45^\circ$ . These diagnostic measures are good indicator of MT forward model accuracy.

The MT method is a frequency sounding technique. An EM signal at a lower frequency penetrates deeper. The depth of penetration ( $d$  in meters), the MT skin depth, can be estimated from the EM signal frequency ( $f$  in Hz) and material resistivity ( $\rho$  in  $\Omega\cdot\text{m}$ ) by:

$$d = 503\sqrt{\rho/f}$$

For example, for a medium of  $100 \Omega\cdot\text{m}$  and a frequency of 100 Hz the skin depth is  $\sim 500$  m, while for the same medium resistivity and the frequency of 1 Hz the skin depth is  $\sim 5$  km.

### 3.7 AMT for conductive targets

Same electrical resistivity models as described in Section 3.5 were used for AMT simulations. Seven MT stations at 100-m spacing were deployed along the center line of the leakage plume (Figure 3.19). Each MT data set consists of apparent resistivity and phase values at 17 frequencies and at seven MT stations.

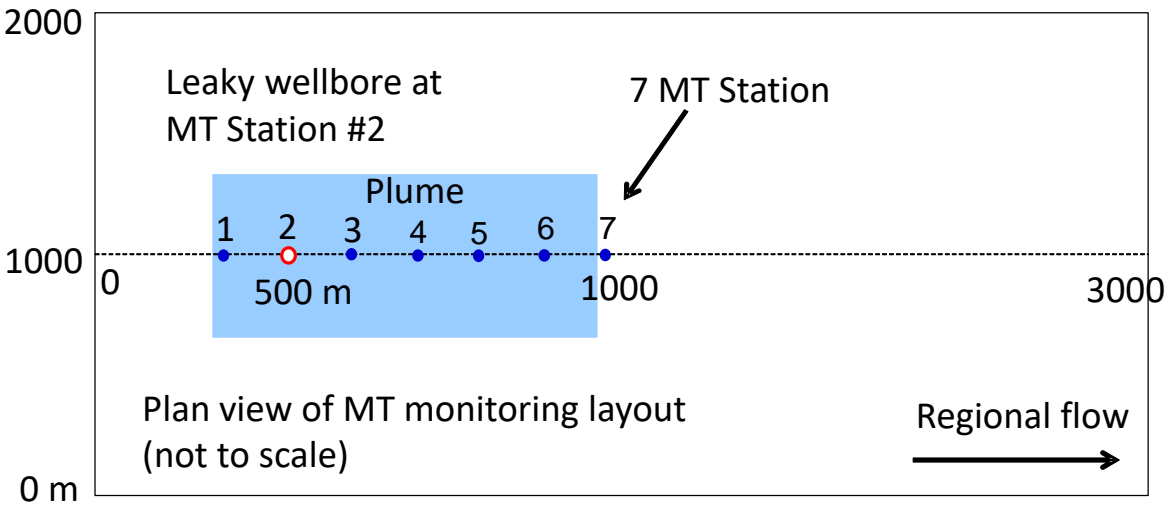


**Figure 3.19.** Locations of seven MT stations at 100-m spacing along the center line of a likely leakage plume.

Brine and CO<sub>2</sub> leakage results in changes in MT apparent resistivity and phase. Figure 3.20 shows this effect at two MT stations (#2 and #5) for the same simulation described in Figure 3.14. It is clear that MT signal changes with time and sensor location. The apparent resistivity is more sensitive to the plume growth than the phase data.

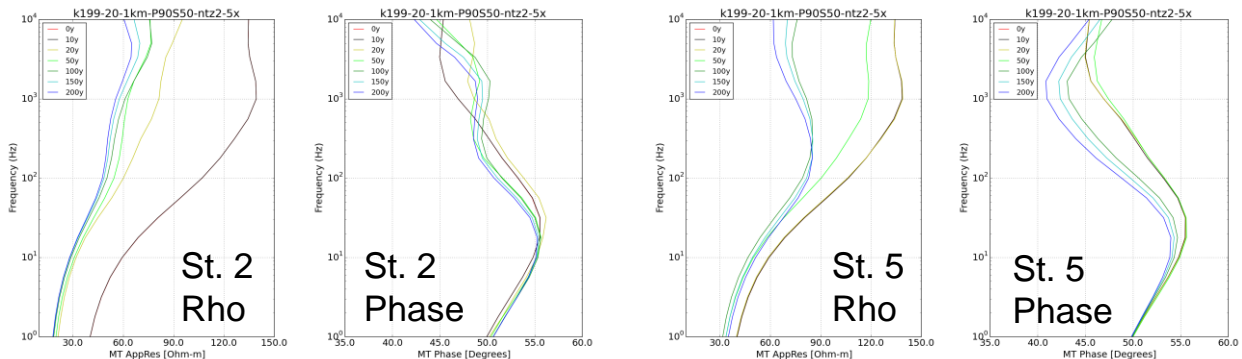


**Figure 3.20.** MT apparent resistivity and phase versus signal frequency at seven time steps and two MT stations (#2 and #5).

Yang et al. (2017a, 2017b) use these ERT and MT datasets to establish links between the plume mass estimated from TDS increase due to the leakage and its depth to the changes in apparent

resistivity and phase. These results are then used to estimate the likelihood of brine and CO<sub>2</sub> leak detection.

### 3.8 References

- Archie, G. E. (1942), The electrical resistivity log as an aid in determining some reservoir characteristics, *T Am I Min Met Eng*, 146, 54-61.
- Buscheck, T. A., K. Mansoor, X. Yang, and S. A. Carroll (2017), Simulated Data for Testing Monitoring Techniques to Detect Leakage in Groundwater Resources: Kimberlina Model with Wellbore Leakage, Rev. 1.1. Report. LLNL-TR-731055, 29 pp, Lawrence Livermore National Laboratory.
- Carroll, S., Y. Hao, and R. Aines (2009), Geochemical detection of carbon dioxide in dilute aquifers, *Geochem T*, 10.
- Chave, A. D., and A. G. Jones (2012), The magnetotelluric method: Theory and practice, Cambridge University Press.
- Commer, M., and Newman, G. A. (2008). New advances in three-dimensional controlled-source electromagnetic inversion. *Geophysical Journal International*, 172, 513-535.
- Garcia, X., and A. G. Jones (2008), Robust processing of magnetotelluric data in the AMT dead band using the continuous wavelet transform, *Geophysics*, 73(6), F223-F234.
- García, X., and A. G. Jones (2005), A new methodology for the acquisition and processing of audio-magnetotelluric (AMT) data in the AMT dead band, *Geophysics*, 70, G119-G126.
- Gueguen, Y. (1994). Introduction to the physics of rocks, Princeton.
- Hoversten, G. M., Commer, M., Haber, E., and Schwarzbach, C. (2015). Hydro-frac monitoring using ground time-domain electromagnetics. *Geophysical Prospecting*, 63, 1508-1526.
- Iliceto, V., and G. Santarato (1999). On the interference of man-made EM fields in the magnetotelluric ‘dead band’, *Geophys Prospect*, 47, 707-719.
- Kelbert, A., N. Meqbel, G. D. Egbert, and K. Tandon (2014). ModEM: A modular system for inversion of electromagnetic geophysical data, *Comput Geosci-Uk*, 66, 40-53.
- LaBrecque, D., and W. Daily (2008), Assessment of measurement errors for galvanic-resistivity electrodes of different composition, *Geophysics*, 73(2), F55-F64.
- Moskow, S., Druskin, V., Habashy, T., Lee, P., and Davydycheva, S. (1999). A finite difference scheme for elliptic equations with rough coefficients using a Cartesian grid nonconforming to interfaces. *SIAM Journal on Numerical Analysis*, 36(2), 442-464.

- Nakatsuka, Y., Z. Xue, H. Garcia, and T. Matsuoka (2010). Experimental study on CO<sub>2</sub> monitoring and quantification of stored CO<sub>2</sub> in saline formations using resistivity measurements. International Journal of Greenhouse Gas Control, 4, 209–216.
- Ogaya Garcia, X. (2014). Magnetotelluric characterisation and monitoring of the Hontomín CO<sub>2</sub> storage site, Spain, University of Barcelona.
- Schmidt-Hattenberger, C., P. Bergmann, T. Labitzke, F. Wagner, and D. Rippe (2016). Permanent crosshole electrical resistivity tomography (ERT) as an established method for the long-term CO<sub>2</sub> monitoring at the Ketzin pilot site, Int J Greenh Gas Con, 52, 432-448.
- Simpson, F., and K. Bahr (2005), Practical magnetotellurics, Cambridge University Press.
- Streich, R., M. Becken, and O. Ritter (2010). Imaging of CO<sub>2</sub> storage sites, geothermal reservoirs, and gas shales using controlled-source magnetotellurics: modeling studies, Chem Erde-Geochem, 70, 63-75.
- Visconti, F., J. M. de Paz, and J. L. Rubio (2010). An empirical equation to calculate soil solution electrical conductivity at 25 degrees C from major ion concentrations, Eur J Soil Sci, 61(6), 980-993.
- Walton, N. (1989). Electrical conductivity and total dissolved solids—What is their precise relationship?, Desalination, 72, 275-292.
- Yang, X., R. N. Lassen, K. H. Jensen, and M. C. Looms (2015). Monitoring CO<sub>2</sub> migration in a shallow sand aquifer using 3D crosshole electrical resistivity tomography, Int J Greenh Gas Con, 42, 534-544.
- Yang, X., T. A. Buscheck, K. Mansoor, and S. A. Carroll (2017a). Magnetotelluric detection thresholds as a function of leakage plume depth, TDS and volume. Report. LLNL-TR-729937, 17 pp, Lawrence Livermore National Laboratory.
- Yang, X., T. A. Buscheck, K. Mansoor, and S. A. Carroll (2017b). Likelihood of brine and CO<sub>2</sub> leak detection using magnetotellurics and electrical resistivity tomography methods. Report. LLNL-TR-738414, 19 pp, Lawrence Livermore National Laboratory.

## (4) METHODOLOGY FOR INCORPORATING ERT MONITORING DATA INTO DREAM

### 4.1 Overview

One purpose of the DREAM tool is to optimize the locations of monitoring sensors for CO<sub>2</sub> leak detection. Electrical conductivity is one property expected to be significantly altered by the presence of CO<sub>2</sub> in the subsurface, making it a useful diagnostic property for CO<sub>2</sub> monitoring. Furthermore, conductivity can be remotely estimated far from sensor locations using ERT, whereby an array of electrodes is used to collect ERT survey data, which is then inverted to estimate the subsurface conductivity distribution (e.g., Bergmann et al., 2017; Carcione et al., 2012; Carrigan et al., 2013; Christensen et al.; 2006, Schmidt-Hattenberger et al., 2016; Commer et al., 2016; Strickland et al., 2014). Given adequate placement of electrodes, changes in conductivity distribution over time derived from time-lapse ERT monitoring may be used to monitor the location of the CO<sub>2</sub> front during injection operations, including the presence of CO<sub>2</sub> in unwanted locations.

For example, Figure 4.1 (top) shows the simulated change in subsurface electrical conductivity above a leaking cap rock zone, and a corresponding wellbore with ERT electrodes grouted in the annulus. Figure 4.1 (bottom) shows the corresponding change in the electrical potential field, given a current injection at the electrode position indicated, with the current sink electrode far from source. Measurement of the change in potential at any location within zone of altered potential (e.g. another electrode within the annulus) would be diagnostic of a potential leak condition. Furthermore, many such measurements in a single borehole can be tomographically inverted to produce an image of the change in conductivity near the borehole. If two boreholes are in relative proximity and instrument with electrodes, then crosshole ERT imaging for leak detection monitoring may be possible, whereby images of changes in conductivity between boreholes are produced. ERT can also be conducted using surface electrodes, although surface deployments have relatively low sensitivity to smaller scale changes in the deep subsurface.

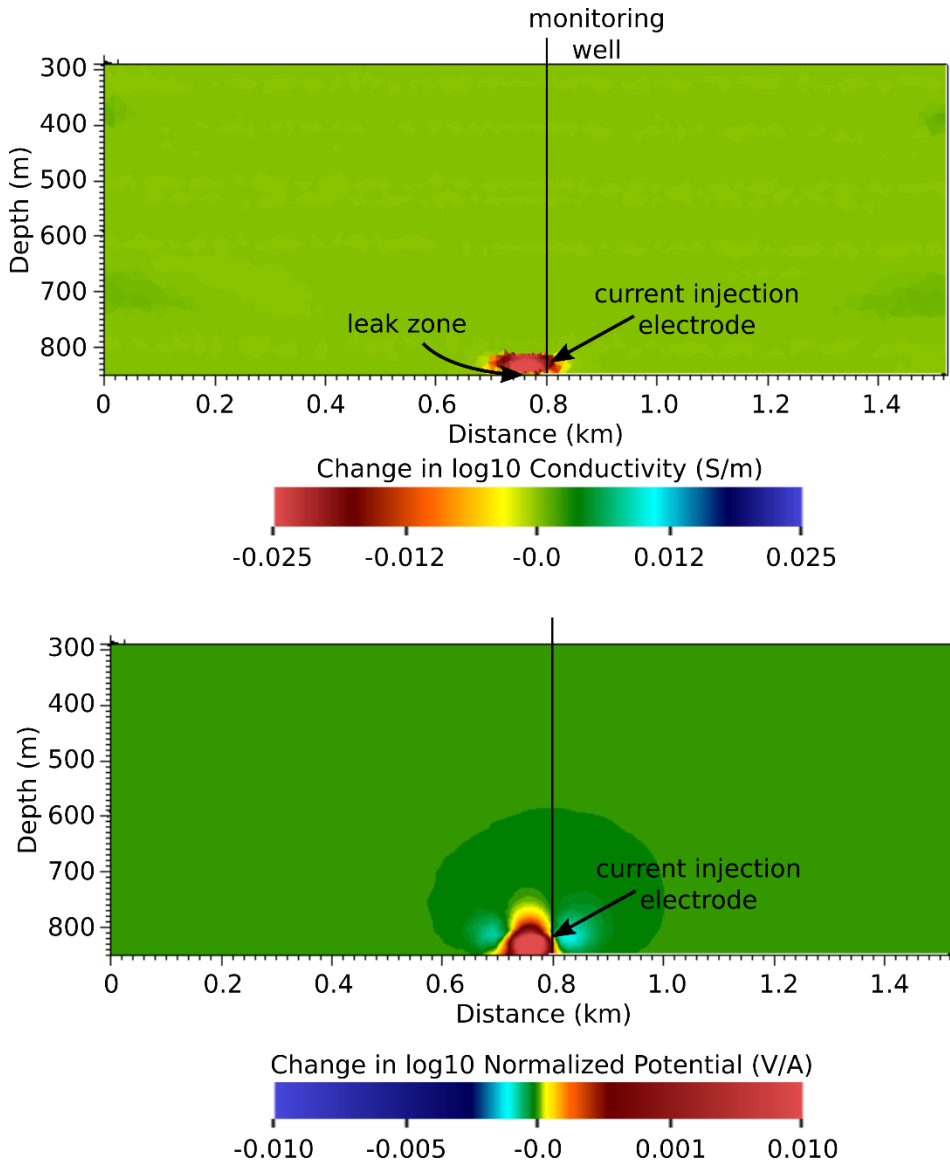


**Figure 4.1.** (top) Simulated change in bulk electrical conductivity caused by a cap rock containment failure. (bottom) Change in subsurface electrical potential a current injection electrode within the wellbore annulus at the position indicated.

The objective is to enable DREAM to incorporate ERT imaging capabilities in its leak detection monitoring optimization routine. To do this, DREAM must be made capable of assessing the utility of ERT for a particular monitoring objective, and the corresponding cost of implementing that capability. Although there are several useful metrics for evaluating the utility of a given ERT array for CO<sub>2</sub> leak detection monitoring (e.g. location of the leak, size of leak zone, rate of leak zone growth, etc.) focus here is on initial leak detection. This represents the first enhancement to DREAM that utilizes geophysical sensing data, and will lay the groundwork for including other

types of geophysical data, and other metrics (e.g., in addition to leak detection) provided by those data.

The following section outlines the strategy and software development that will enable DREAM to assimilate ERT data in a computationally tractable manner. To do this, DREAM will be loosely coupled with E4D (Johnson et al., 2010), a highly parallel ERT modelling and inversion tool. The resulting DREAM-E4D module will ingest data from DREAM, simulate ERT survey responses, and produce a matrix of estimated detection times for a given leak simulation scenario and set of candidate wellbore locations. DREAM-E4D simulations are expected to be computationally intensive, but tractable on modern multi-core workstations. Therefore, DREAM-E4D will run independently of the DREAM tool, but will provide output files (e.g., leak detection matrices) that will later be assimilated by the DREAM tool during wellbore placement optimization calculations.

## 4.2 DREAM-E4D Workflow

1. In the first step DREAM produces a set of output files describing the parameters for a particular leak scenario simulation that are necessary to compute the spatio-temporal evolution of bulk electrical conductivity. These parameters include the mesh dimensions and petrophysical function inputs such as porosity, concentrations of primary ionic phases, ionic strength, total dissolved solids, and Archie's Law parameters (saturation exponent and cementation factor). DREAM will also provide the candidate set of wellbore locations for the current simulation. For a given wellbore configuration, it is likely that ERT survey data will be sensitive to changes in conductivity due to expansion of the primary plume during injection. For this reason, it is necessary to have baseline simulations results that describe the scenario response under no-leak conditions, in addition to the leak condition simulation results. Both simulations are necessary to enable the DREAM-E4D module to isolate the changes in ERT data that are attributable to the leak. Those changes in (simulated) ERT data will ultimately be used to determine the leak detection time for a wellbore set.

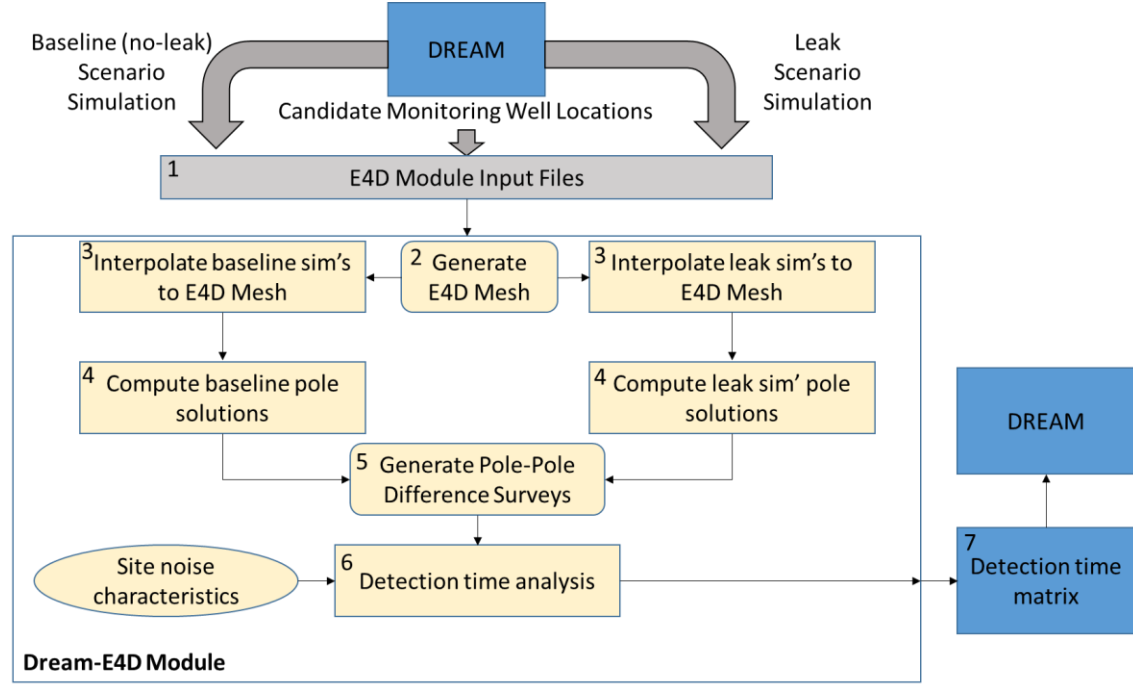


**Figure 4.2. DREAM-E4D Flow Diagram**

2. In step 2 the DREAM-E4D module will construct the E4D simulation mesh based on the flow and transport simulation grid provided by DREAM and the candidate wellbore locations. Wellbore electrode points will be incorporated into the mesh based on a pre-determined vertical spacing interval.
3. In step 3 the baseline and leak scenario simulation results will be interpolated to the E4D mesh. Prior to interpolation, parameters provided by DREAM in the E4D input files will be transformed to bulk electrical conductivity on the simulation grid. Interpolation to the E4D mesh will be using an open source parallel mesh interpolation library called Data Transfer Kit, which was developed by University of Madison Wisconsin and Oakridge National Laboratory.
4. The primary computational burden of the E4D module will be addressed in step 4, wherein the pole solutions are computed for each electrode and each flow simulation time step. The pole solution for a given electrode is the electrical potential field produced when that electrode is used as the current source, with the current sink at infinite distance from the source. Using the principle of superposition, the set of pole solutions can be used to reconstruct any possible ERT measurement given the current set of candidate monitoring wells, and therefore contains all of the information that can potentially be provided by that set of wells in terms of ERT imaging.

5. ERT imaging resolution is naturally dependent on the set of ERT measurements used to produce a given image. For N electrodes, the number of unique measurements that can be collected is  $N*(N-1)*(N-2)*(N-3)/8$ . Collecting every measurement quickly becomes untenable as the number of electrodes increases. Designing ERT surveys for optimal resolution is an area of active research, and currently proposed methods would be computationally prohibitive in DREAM-E4D. Therefore two assumptions are made: 1) ERT imaging will be conducted using either a single monitoring well, or a pair of monitoring wells (i.e., 1D or 2D), and 2) all ERT imaging surveys will be pole-pole surveys. Pole-Pole surveys assume four electrode measurements with the current sink and negative potential electrode at infinite distance. Under noise-free conditions, pole-pole surveys provide all of the information available for a given set of electrodes. However, in the presence of noise, the pole-pole survey typically doesn't not provide optimal sensitivity to changing conditions, or optimal imaging resolution. Therefore, use of the pole-pole survey for estimating detection time is considered conservative. In step 5, the DREAM-E4D module uses the pole solutions to reconstruct the pole-pole surveys for each well alone, for each wellbore pair in the candidate set of wellbores, and for each time-step in the simulation. The baseline survey is then subtracted from the leak simulation at each time-step to produce the change in pole-pole survey data caused by the leak condition at each time-step.
  
6. In step 6 the pole-pole difference surveys generated in step 5 are used to estimate the time of detection for each ERT imaging option (single well or wellbore pair). One approach for estimating detection time is to invert each survey at each time-step, and then to determine when changes in conductivity appear outside of the intended reservoir using a change detection algorithm. However, given the computational demands of ERT inversion, this approach is computationally untenable. Instead, the pole-pole difference surveys and, an assumed data change threshold are used to determine when CO<sub>2</sub> would be apparent in the image outside of the primary reservoir (i.e., in the leak zone). For example, the change detection time for a given wellbore pair is the time at which 10% of the pole-pole difference data reach 120% of the noise threshold for a given measurement. Because these changes are caused by the CO<sub>2</sub> leak alone, it is assumed that fitting those data in the inversion will require a corresponding change in conductivity in the region of the leak (within the limits of imaging resolution), thereby indicating a leak in the corresponding ERT image. As part of step 6, an inverse analysis will be executed on select surveys to verify that actual detection times occur before or at the estimated detection time.
  
7. In step 7 all of the simulation results, and corresponding estimated detection times, are synthesized into a single matrix, one for each leak scenario. Each axis of the matrix will represent monitoring wellbore numbers. If (i,j) represents the matrix index, then element (i,j)

represents the detection time for wellbore  $i$  if  $i = j$ , and the detection time for wellbore pair  $(i,j)$  if  $(i \neq j)$ .

Step 7 represents the completion of DREAM-E4D computations. One detection matrix is produced for each leak scenario. In the next step, DREAM uses each matrix to stochastically determine optimal wellbore locations in terms of leak detection time based ERT sensing capabilities in addition to other sensing modalities that are under consideration and accommodated by DREAM.

### 4.3 References

- Bergmann, P., Schmidt-Hattenberger, C., Labitzke, T., Wagner, F.M., Just, A., Flechsig, C. and Rippe, D. (2017). Fluid injection monitoring using electrical resistivity tomography five years of CO<sub>2</sub> injection at Ketzin, Germany, Geophys Prospect, 65, 859-875.
- Carcione, J.M., Gei, D., Picotti, S. and Michelini, A. (2012). Cross-hole electromagnetic and seismic modeling for CO<sub>2</sub> detection and monitoring in a saline aquifer, J Petrol Sci Eng, 100, 162-172.
- Carrigan, C.R., Yang, X.J., LaBrecque, D.J., Larsen, D., Freeman, D., Ramirez, A.L., Daily, W., Aines, R., Newmark, R., Friedmann, J., and Hovorka, S. (2013). Electrical resistance tomographic monitoring of CO<sub>2</sub> movement in deep geologic reservoirs, Int J Greenh Gas Con, 18, 401-408.
- Christensen, N.B., Sherlock, D., and Dodds, K. (2006). Monitoring CO<sub>2</sub> injection with cross-hole electrical resistivity tomography, Explor Geophys, 37, 44-49.
- Commer, M., Doetsch, J., Dafflon, B., Wu, Y.X., Daley, T.M., and Hubbard, S.S. (2016). Time-lapse 3-D electrical resistance tomography inversion for crosswell monitoring of dissolved and supercritical CO<sub>2</sub> flow at two field sites: Escatawpa and Cranfield, Mississippi, USA, Int J Greenh Gas Con, 49, 297-311.
- Johnson, T.C., Versteeg, R.J., Ward, A., Day-Lewis, F.D., and Revil, A. (2010). Improved hydrogeophysical characterization and monitoring through parallel modeling and inversion of time-domain resistivity and induced-polarization data, Geophysics, 75, Wa27-Wa41.
- Schmidt-Hattenberger, C., Bergmann, P., Labitzke, T., Wagner, F., and Rippe, D. (2016). Permanent crosshole electrical resistivity tomography (ERT) as an established method for the long-term CO<sub>2</sub> monitoring at the Ketzin pilot site, Int J Greenh Gas Con, 52, 432-448.
- Strickland, C.E., Vermeul, V.R., Bonneville, A., Sullivan, E.C., Johnson, T.C., Spane, F.A., and Gilmore, T.J. (2014). Geophysical Monitoring Methods Evaluation for the Future Gen 2.0 project, Enrgy Proced, 63, 4394-4403.

## SUMMARY

The use 4D seismic to monitor injected CO<sub>2</sub> was best demonstrated by the Sleipner project which has been conducting 3D seismic surveys over an increasing volume of injected CO<sub>2</sub> since the mid 1990's. In this report, we focus on early detection of CO<sub>2</sub> leakage from the storage reservoir, which means imaging much smaller volumes of CO<sub>2</sub> than in Sleipner case. Determining the velocity model (a 3D description of velocity in the subsurface) is crucial to proper use of seismic data. The seismic velocity depends on the bulk and shear modulus and density (see rock physics section). These three parameters uniquely determine both P-wave and S-wave velocities for isotropic media. Inversely, obtaining P-wave and S-wave velocities from seismic monitoring data allows determination of elastic moduli (e.g., bulk and shear moduli) and density. Then, using rock physics relationships; reservoir parameters such as fluid saturation, porosity and pressure can be determined from the elastic moduli. In practice, the use of seismic monitoring data to understand reservoir properties is usually a loop between modeling of the data and processing/analysis of the data. Because of the large number of reservoir properties impacting the seismic response, as well as varying complexity in rock physics models, forward modeling is important to increase confidence in quantitative interpretations.

Sections 1.5-1.7 describe workflow for forward modeling of seismic data and seismic data processing. The elastic parameters used in the rock physics modeling have significant effects on the constructed seismic velocity model and the generated synthetic seismic data. The uncertainties in the estimated seismic responses could be largely attributed to the uncertainties in these elastic parameters, especially the bulk and shear moduli of clay minerals. The model used to demonstrate the steps had a very small CO<sub>2</sub> plume, and therefore the responses were very small, and not detectable under realistic field conditions. Applying this approach to models with different plume sizes will establish detection limits and identify scenarios for which this technique would be effective.

Section 1.8 describes an approach when inhomogeneity, e.g., fault might play a significant role in a storage reservoir behavior and it is necessary to image the subsurface with a higher accuracy. On the other hand, Section 1.9 describes a tool for fast detection and location of induced microseismic events due to CO<sub>2</sub> injection that may result in stress and/or pore-pressure changes.

Gravity monitoring can be used to map subsurface density distribution by measuring changes in the local gravitational field either on the ground surface or in boreholes. Since the density of CO<sub>2</sub> is less than that of the brine, replacing the original fluid contained in the pores of the rock matrix by CO<sub>2</sub> will produce a bulk density decrease, which in turn will produce perturbations in the measured local gravitational field. Similar to seismic monitoring, the model used to demonstrate the steps of gravity modeling produced small signals on the surface that might not be

measureable with current technology in realistic field conditions. The example of the response in nearby well showed the signal that would clearly indicate to location of CO<sub>2</sub> plume.

The electrical resistivity of the subsurface is highly sensitive to changes in formation properties such as porosity, pore fluid resistivity, and fluid saturation. Electrical and EM techniques infer the distribution of electrical resistivity in the subsurface from measured electric and magnetic fields. The resistivity of CO<sub>2</sub> is high, similar to gas or air, while the resistivity of brine in storage formations that are hydrologically separated from drinking water reservoirs is low. A finite size CO<sub>2</sub> plume would produce a resistivity contrast with the enclosing formation. The replacement of highly conductive (low resistivity) saline fluids with resistive CO<sub>2</sub> results in resistivity increase in the storage reservoir. When CO<sub>2</sub> is present at shallow depths, dissolution of CO<sub>2</sub> causes increase in TDS and results in resistivity decrease. Resistivity techniques are much more sensitive to low resistivities (conductive targets), and hence deep resistive targets are much more difficult to detect. Examples in Section 3.2 and 3.3 illustrate that the response to a shallow conductive target is an order of magnitude larger than to the deep resistive target. There are many possible configurations of sources (transmitters) and receivers (sensors). Configurations in Sections 3.2-3.5 use an active source, while MT described in Section 3.6 uses a natural source. The advantage of passive techniques (e.g., MT) is an ease of deployment in the field, and that there are no source/configuration artifacts present in the data. However, as the natural field strength varies, the signals might not be strong enough to produce large enough signals from the regions of interest. The configurations using the active source can be optimized for required spatial resolution, but the field deployment is more expensive and advanced data processing is required.

One of the DREAM tool capabilities is to optimize locations of monitoring sensors for CO<sub>2</sub> leak detection. Section 4 describes efforts to enable DREAM to incorporate ERT imaging capabilities in its leak detection monitoring optimization routine. This represents the first enhancement to DREAM that utilizes geophysical sensing data, and will lay the groundwork for including other types of geophysical data, and other metrics (e.g., in addition to leak detection) provided by those data.

## ACRONYMS

1D	One-dimensional
2D	Two-dimensional
3D	Three-dimensional
4D	Time being the fourth dimension
AMT	Audio-frequency Magnetotellurics
B	Magnetic field
CSAMT	Controlled Source Audio Magnetotellurics
CSEM	Controlled Source ElectroMagnetics
CMP	Common Midpoint Gather
CO <sub>2</sub>	Carbon Dioxide
DC	Direct Current
DREAM	Designs for Risk Evaluation and Management
E	Electric field
EC	Electrical Conductivity
EM	Electromagnetic
ERT	Electrical Resistance Tomography
H	Magnetic Field ( $B = \mu H$ )
MT	Magnetotellurics
ROM	Reduced Order Model
STOMP	PNNL Flow Simulator
TDS	Total Dissolved Solids
TOUGH2	LBNL Flow Simulator
TTI	Tilted Transverse Isotropic
VRH	Voigt-Reuss-Hill (averaging of mineral constituents)
VSP	Vertical Seismic Profile
Z	Impedance tensor

## **ACKNOWLEDGMENTS**

This work was completed as part of National Risk Assessment Partnership (NRAP) project. Support for this project comes from the U.S. Department of Energy (DOE) Office of Fossil Energy's Crosscutting Research Program. Work at Lawrence Berkeley National Laboratory was completed under the U.S. DOE Contract No. DE-AC02-05CH1123. Work at National Energy Technology Laboratory was performed under Field Work Proposal No. 1022407. Work at Los Alamos National Laboratory was supported under the U.S. DOE Contract No. DE-AC52-06NA25396. Work at Pacific Northwest National Laboratory was supported under the U.S. DOE Contract No. DE-AC05-76RL01830. Work at Lawrence Livermore National Laboratory was performed under the U.S. DOE Contract No. DE-AC52-07NA27344.